UNIVERSITÀ DEGLI STUDI DI PADOVA

DEPARTMENT OF INDUSTRIAL ENGINEERING

MASTER'S DEGREE IN MECHANICAL ENGINEERING

Large Eddy Simulations of a supersonic turbulent boundary layer

Candidate:
Tommaso PIZZATI

Thesis advisor:
Ing. **Francesco DE VANNA**, PhD

Thesis co-advisor:
Prof. **Francesco PICANO**

ACADEMIC YEAR 2019/20

Science is made up of mistakes, but they are mistakes which it is useful to make, because they lead little by little to the truth.

JULES VERNE, *A journey to the centre of the Earth*

to my family and loved ones

Sommario

In questa tesi viene proposta una campagna di simulazioni numeriche mediante la tecnica Large Eddy Simulation (LES) di uno strato limite supersonico e turbolento su di una lastra piana.
Tale lavoro vuole in primo luogo analizzare la turbolenza di parete ed ispezionare i parametri di griglia che più influenzano l'accuratezza della soluzione in tale ambito.
Lo studio viene effettuato in termini di moto medio (profili wall-normal della velocità media streamwise) e fluttuazioni (profili degli sforzi di Reynolds).
Viene dunque proposta un'analisi LES con approccio wall-resolved (WRLES) al variare della risoluzione di griglia lungo le direzioni streamwise, spanwise e al variare della dimensione del dominio lungo la direzione spanwise.
Si considera inoltre lo sviluppo del coefficiente d'attrito e del numero di Reynolds d'attrito stesso lungo la lastra.
Ciascun andamento viene confrontato con dati DNS di riferimento.
Si propone, inoltre, un'analisi LES mediante approccio wall-modelled (WMLES) al variare della risoluzione di griglia lungo la direzione wall-normal, utilizzando un modello di parete di tipo algebrico appositamente realizzato.
Tali risultati vengono confrontati con quanto ottenuto mediante un noto modello di parete differenziale proposto da Kawai e Larsson e con i dati DNS di riferimento.
I risultati WRLES appaiono accurati, e sottolineano una forte sensibilità della soluzione al variare della risoluzione di griglia lungo le direzioni spanwise e streamwise, mentre si osserva la quasi indipendenza della soluzione al variare della dimensione del dominio in direzione spanwise.
Per quanto concerne l'analisi WMLES, si ottengono profili coerenti con quelli DNS e quasi coincidenti con quelli ottenuti con il modello differenziale, anche a bassa risoluzione.
Tale studio risulta dunque particolarmente interessante, mettendo in luce risultati significativi soprattutto nel campo WMLES.
Tale tecnica viene dunque confermata come molto promettente nell'ambito della turbolenza di parete, grazie a risultati dignitosi in relazione ad un conveniente rapporto tra qualità dei risultati e tempo di simulazione.

Abstract

This thesis deals with the analysis of a supersonic turbulent boundary layer on a flat plate through several numerical simulations using a Large Eddy Simulation (LES) approach.
Firstly such work aims to analyse the wall turbulence and to inspect the grid features which have a great influence on the solution in the proposed framework.
The study is carried out in terms of mean motion (wall-normal profiles of the streamwise mean velocity) and fluctuations (Reynolds stress).
So a wall-resolved LES (WRLES) simulations campaign is proposed as the grid resolution varies along the streamwise and spanwise directions and as the domain size changes along the spanwise direction.
Moreover, also the growth of the friction factor and of the friction Reynolds number is considered.
Results are compared to the reference DNS data.
Secondly, we want to propose a LES analysis with a wall-modelled approach (WMLES) as the grid resolution varies along the wall-normal direction, using an algebraic wall model realised for this study.
Results are compared to those ones obtained by means of a differential wall model proposed by Kawai and Larsson and with DNS reference data.
The WRLES results are really accurate, and they highlight the strong sensitivity of the solution as the resolution grid varies along streamwise and spanwise directions, while on the other hand they emphasise the almost solution's independence as the domain size varies along the spanwise direction.
Regarding the WMLES analysis to varying of the resolution along the wall-normal direction, results are consistent with the DNS ones and almost coincident with those ones obtained with the differential model.
Hence, this work appears really interesting, with particular reference to the WMLES results.
Such technique is confirmed as really promising in the wall turbulence field, thanks to significant results related to a decent ratio between results quality and simulation time.

Acknowledgements

First and foremost, I would like to express my sincere gratitude to my advisor, Ing. Francesco De Vanna, for the opportunity and for his support during these last months. It has been a real pleasure working on my thesis, thanks to the cordiality and the helpfulness shown.
I would like to extend my appreciation also to my co-advisor, for his kindness and for his advices.
I would like to thank all my friends and university colleagues. It was a privilege to meet such true and accomodating persons.
My special thanks are due to my girlfriend, for his support and his patience even during difficult periods.
Lastly, and most certainly not least, I would like to express my deep thanks to my parents and my brother. It's thanks to them if I'm standing where I am now. I'm really glad of having these persons by my side.
I intend to treasure every moment of this growth path. I will cherish it forever.

Nomenclature

AWS Algebraic Wall-Stress

DES Detached Eddy Simulation

DNS Direct Numerical Simulation

DWS Differential Wall-Stress

LES Large Eddy Simulation

$LODI$ Local One Dimensional Inviscid

NS Navier-Stokes

$NSCBC$ Navier-Stokes Characteristic Boundary Conditions

ODE Ordinary Differential Equations

$RANS$ Reynolds Averaged Navier-Stokes

SGS Subgrid-scale

TBL Turbulent Boundary Layer

$URANOS$ Unsteady Robust All-around Navier-Stokes Solver

$WALE$ Wall-Adapting Large Eddy

$WMLES$ Wall-Modeled Large Eddy Simulation

$WRLES$ Wall-Resolved Large Eddy Simulation

Contents

Chapter 1

Introduction

Despite being a canonical flow, the turbulent boundary layer on a flat plate remains a subject of interest.
From a practical point of view, the knowledge of such kind of flows at high Mach numbers is essential for the design of high-speed vehicles.
For example, high-performance ballistic vehicles are subject, during re-entry, to an intense fluctuating pressure field which can affect the integrity of the vehicle structure and may impose adverse vibration levels on internal components.
These pressure fluctuations arise from instability and unsteady motions of fluid which focus on intermittent eruptions of the viscous sublayer [17].
Furthermore, these vehicles require powerful propulsion systems that increase the severity of the loading in the engine inlet and exhaust regions [23].
Shock impingement may also occur, with a local intensification of loads.
So, turbulent boundary layer produces significant fluid dynamic and thermal loads over the majority of the outer skin, determining the aerodynamic drag and the heat transfer [44].
Pressure fluctuations within the boundary layer are very important not only in this framework since, in general, they are a dominant cause of damaging effects such as acoustic fatigue and flutter of structural elements [31, 5].
Since the 1950s and the development of more powerful gas turbine engines, there has been an increase in the number of reported fatigue failures of aircraft skin structures [32].
Wings of airplanes, pressure hulls of submarines, trains, are all composed of stiffened structures that are excited by pressure fluctuations due to the turbulent flow induced by their movement [19].
In transonic and supersonic axial-flow compressor or fan, blades may show fatigue failures because of excitation at the resonance frequencies due to localized stall: this is an aerodynamic phenomenon, where loss of continuity in the flow lines results in the formation of vortices, flow reversal and turbulence [2].
Moreover, shock waves can be observed into this kind of turbomachines.
In particular, the interaction between such waves and the blades boundary layer can magnify the adverse pressure gradient magnitude: consequently, the boundary layer thickness increases faster and this can eventually result in reverse flow, generating a separation bubble and contributing to the aerodynamic losses.
Furthermore, such interaction could also result in the buffeting phenomenon, that is, a shock wave instability, which is responsible for the creation of aeroelastic loads on the blades and vibrations stresses [11].
Thus it's important to understand the dynamics of turbulent boundary layers and how a stiffened structure reacts to TBL excitation.
In this work we want to study such kind of wall-flow using Large eddy simulations.
Large eddy simulation (LES) approach is gaining ground more and more in the last few years in turbulence research, thanks to more accurate results compared to the Reynolds Averaged Navier

Stokes (RANS) technique, but lower computational cost than Direct Numerical Simulations (DNSs). Furthermore, it is turning out to be a promising alternative also in industrial field for the near future.
One of the most important limits of such an approach is the simulation of turbulent boundary layer, because its computational cost becomes highly prohibitive, especially at high Reynolds number.
Boundary layers are multi-scale phenomena where the energetic motions in the inner layer (that are responsible of the kinetic energy production) become smaller in size as the Reynolds number increases. Hence, the required grid resolution scales with the viscous length scale if the goal is to solve the inner layer.
More in detail, such area is dominated by near-wall coherent structures (e.g. quasi-streamwise vortices, velocity streaks, sweep, ejection and burst events) that are closely connected to turbulence production and to large wall shear stress [22].
These structures exhibit low and high-speed streaks in the near wall region [16], arranged alternately along the spanwise direction (with an averaged spacing of 100 wall units) and elongated longitudinally (with an average length of 1000 wall units) in the buffer layer [3].
Velocity streaks, together with turbulent events, are directly linked to quasi-streamwise vortices [34]: the first contain most of the turbulent kinetic energy, the latter organize both the energy dissipation and Reynolds stresses [13].
Thus, such complexity in structures organization results in high computational resources required to numerically reproduce the correct dynamics.
Hence, in view of wall-resolving approach, the main point becomes the grid-nodes distribution evaluation which permits to have the best compromise between accuracy and computational cost.
However, there have been proposed several alternative solutions to the resolving technique, whose aim is to model the turbulence in the inner part of the boundary layer.
Therefore there's no need to resolve the dynamics next to the wall, which are really heavy for the simulation.
These methods differ in terms of philosophy, computational cost and potential accuracy.
Considering a flow over an airfoil, different regions can be detected: the detached shear layer, the outer part and the inner part of the boundary layer.
An important distinction is that *Wall-Modelled LES* (WMLES) resolves energetic motions both in the detached shear layer and outer layer, while *Detached Eddy Simulation* (DES) only resolves those in the first region.
The state of the wall-modelling fields up to the early-to-mid 2000s was reviewed by Piomelli and Balaras [28], Sagaut [33], and Piomelli [27].
In addition to that, the state of DES was reviewed recently by Spalart [38].
The focus of this thesis is to investigate the difference of accuracy obtained by varying grid resolution and domain size in relation to the relative computational cost, adopting a wall-resolving approach.
Moreover, an algebraic wall-stress model is proposed in order to analyse results by modifying the wall-normal grid resolution: these are then compared to those ones obtained with a differential wall-stress model by Kawai and Larsson, realized for turbulent channel flows and readapted for turbulent boundary layer.

The present analyses have been carried out with URANOS [9, 8].

Chapter 2

LES Governing Equations

2.1 Fundamentals

Large-eddy simulation relies on the idea that small scales of the turbulent flow structure are modelled to obtain a desired reduction in the range of scales required for numerical simulation: therefore only the largest scales (that are the most energetic ones) are simulated [10].
Such an approach can be justified since small scales of the flow are supposed to be more universal and so less determined by boundary conditions than the large ones, according to the local isotropy hypothesis by Kolmogorov.
Thus it's reasonable that a similar technique permits to reduce the computational cost compared to DNS, thanks to the solution of a smaller range of scales than the full one.
Furthermore, it still guarantees much higher accuracy compared to RANS results.
Anyway, this approach requires fields that are in general three-dimensional and time-varying as DNS, so it's surely much expensive in terms of computational cost than RANS.
As all simulation techniques, LES consists in solving a set of governing equations, usually the filtered Navier-Stokes equations with some additional ones, basing on the use of a computational grid, that permits to discretize the fluid domain.
Spatial distribution of the computational grid nodes generates a scale separation, since scales smaller than the grid spacing can't be captured.
Consequently, two subranges of scales are defined:

- *resolved scales*, which are scales large enough to be captured on the grid and represented in the numerical solution;
- *modelled scales*, which are scales too small to be represented on the grid, so they must be described with a dedicated model

It is also worth noting that resolved scales as large as the mesh size may be corrupted by numerical errors. [10]

In summary, given a grid spacing $\Delta \gg \eta$, with η dimension of the Kolmogorov scales, there will be scales with characteristic dimension:

- $l \geqslant \Delta$, to simulate;
- $\eta \ll l \ll \Delta$, to model

Therefore, one of the problems in the field of LES is to define the separation of these subranges and to write governing equations for associated scales.

Several mathematical models have been proposed to overcome such problem since Leonard in 1973, who introduced the filtering concept for removing small scales to LES [10].

2.2 Filtering Operator

In the ideal case of homogenous turbulence, the filter should respect the physical properties of isotropy and homogeneity.
Hence, the filter features are independent of the position and of the orientation of the reference frame.
In this framework, scales are separated using a filter that represents a low-pass filter in frequency.
Formally, a filtering operation is defined to decompose a time-space variable **Q**(**x**,t) into the sum of a filtered (or resolved) component $\overline{\mathbf{Q}}$(**x**,t) and a residual (or subgrid-scale, SGS) component **q**'(**x**,t).[24]
In the case of the velocity field **U**(**x**,t), the *filtered velocity field* $\overline{\mathbf{U}}$(**x**,t), three-dimensional and time-dependent, represents the motions of the large eddies.

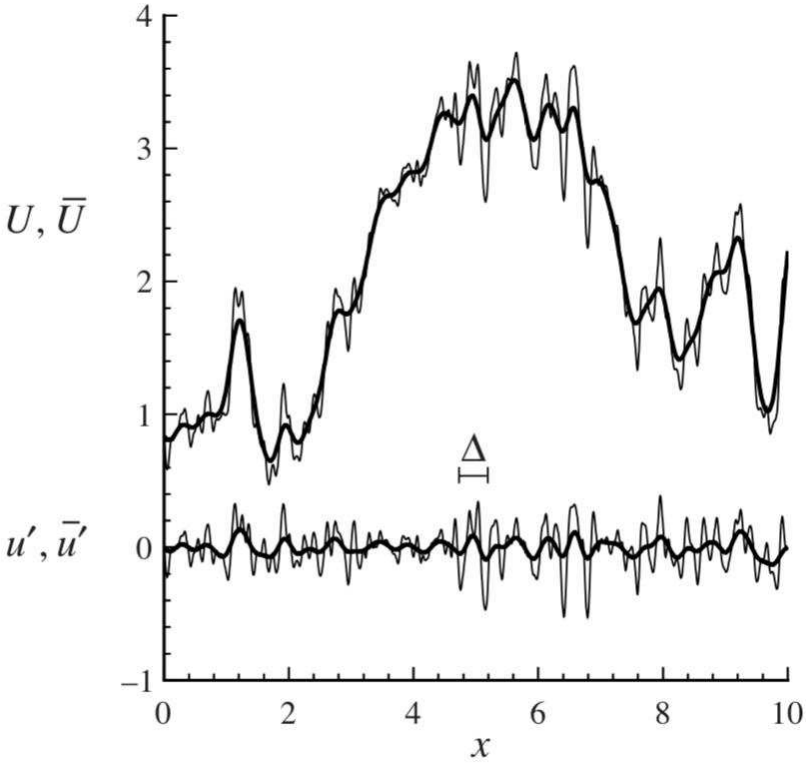

Figure 2.1: Velocity field decomposition in a LES [24]

It is worth noting that, if the filtering operation is applied to the residual component, a field $\overline{\mathbf{u}'}$ is obtained, not null in general.
Filtering is mathematically represented in physical space as a convolution product.
The resolved part $\overline{\mathbf{U}}$(**x**,t) is defined as:

$$\overline{\mathbf{U}}(\mathbf{x},t) = \int G(\mathbf{r},\mathbf{x})\mathbf{U}(\mathbf{x}-\mathbf{r},t)d\mathbf{r} \tag{2.2.1}$$

where the convolution kernel is characteristic of the filter used, and Δ is his spacing (or filter scale).
More briefly, it's possible to write:

$$\overline{\mathbf{U}}(\mathbf{x},t) = G_{\Delta}(\mathbf{U}) \tag{2.2.2}$$

Another important property is the consistency, according to which:

$$\int G(\mathbf{r}, \mathbf{x}) d\mathbf{r} = 1 \tag{2.2.3}$$

There are several convolution filters in literature: most common are proposed in table 2.2.

Name	Filter function
General	$G(r)$
Box	$\frac{1}{\Delta} H(\frac{1}{2}\Delta - \lvert r \rvert)$
Gaussian	$\left(\frac{6}{\pi\Delta^2}\right)^{1/2} \exp\left(-\frac{6r^2}{\Delta^2}\right)$
Sharp spectral	$\frac{\sin(\pi r/\Delta)}{\pi r}$

Figure 2.2: Several kinds of convolution filters

It's important to notice that the grid spacing Δx_i must be minor or eventually equal to the filter scale Δ along a given axis

$$\Delta x_i \leq \Delta$$

in order to take advantage of the separation between scales made by the filter.
If $\Delta x_i = \Delta$, the grid itself is carrying out the role of the filter: this is an example of box filter (or top-hat filter).

2.3 Filtered Conservation Equations

The conservation equations that govern the filtered velocity field $\overline{\mathbf{U}}$(**x**,t) can be obtained by applying the filtering operation to the compressible Navier-Stokes equations.
We want to carry out the development of such equations in non-dimensional formulation, so, the latter must be defined.
Following the Π theorem and the dimensional analysis, we can assume the heat capacity ratio, the free-stream Mach number, the Reynolds number and the Prandtl number as fundamental groups that describe the system.
They can be expressed as combination of the reference parameters describing the problem (whose choice is arbitrary): we use t_0, L_0 as the reference length, ρ_0 as the reference density, $u_0 = \sqrt{p_0/\rho_0}$ as the reference speed (consisting in the speed of sound apart $\sqrt{\gamma_0}$), p_0 as the reference pressure, T_0 as the reference temperature, E_0 as the reference total energy, μ_0 as the reference molecular viscosity, λ_0 as the reference thermal conductivity, R_0 as the reference gas constant, c_{p0} and c_{v0} as the reference specific heats at constant pressure and constant volume respectively, e_0 as the reference internal energy, Pr_0 as the reference Prandtl number, γ_0 as the reference specific heat ratio.

These parameters are related by seven equations:

$$p_0 = \rho R_0 T_0, \qquad \mu_0 = T_0^{\frac{3}{2}}\Big(\frac{T_0+S}{T_0+S}\Big), \tag{2.3.1}$$

$$k_0 = \frac{\mu_0 c_{p0}}{Pr_0}, \qquad e_0 = c_{v0} T_0, \tag{2.3.2}$$

$$E_0 = e_0 + \frac{1}{2}u_0^2, \qquad c_{v0} = \frac{R_0}{\gamma 0 - 1}, \tag{2.3.3}$$

$$c_{p0} = \frac{\gamma_0 R_0}{\gamma_0 - 1} \tag{2.3.4}$$

Let us introduce the following change of variables:

$$x = L_0 x^*, \qquad u_i = u_0 u_i^*, \qquad t = \frac{L_0}{u_0} t^*, \qquad \rho = \rho_0 \rho^*, \qquad T = T_0 T^* \tag{2.3.5}$$

$$e = \frac{p_0}{\rho_0} e^*, \qquad E_{tot} = \frac{p_0}{\rho_0} E_{tot}^*, \qquad \mu = \mu_0 \mu^*, \qquad \lambda = \lambda_0 \lambda^* \tag{2.3.6}$$

where $(\cdot)^*$ stands for a non-dimensional quantity.
Defining the non-dimensional groups as

$$\gamma = \frac{c_{p0}}{c_{v0}} \qquad \text{heat capacity ratio} \tag{2.3.7}$$

$$M_\infty = \frac{u_\infty}{\sqrt{\gamma p_0/\rho_0}} \qquad \text{free-stream Mach number} \tag{2.3.8}$$

$$Re = \frac{\rho_0 u_\infty L_0}{\mu_\infty} \qquad \text{Reynolds number} \tag{2.3.9}$$

$$Pr = \frac{c_{p0}\mu_\infty}{\lambda_\infty} \qquad \text{Prandtl number} \tag{2.3.10}$$

omitting from now on till the end of the chapter the $(\cdot)^*$ to get a smoother reading, the compressible Navier-Stokes equations in non-dimensional formulation result [6] [42]:

$$\begin{cases} \dfrac{\partial \rho}{\partial t} + \dfrac{\partial(\rho u_j)}{\partial x_j} = 0 \\ \dfrac{\partial(\rho u_i)}{\partial t} + \dfrac{\partial(\rho u_i u_j)}{\partial x_j} = -\dfrac{\partial p}{\partial x_i} + \dfrac{\sqrt{\gamma} M_\infty}{Re}\dfrac{\partial(\mu d_{ij})}{\partial x_j} \\ \dfrac{\partial(\rho E)}{\partial t} + \dfrac{\partial(\rho E u_j)}{\partial x_j} = -\dfrac{\partial(p u_j)}{\partial x_j} - \dfrac{c_p \sqrt{\gamma} M_\infty}{RePr}\dfrac{\partial q_j}{\partial x_j} - \dfrac{\sqrt{\gamma} M_\infty}{Re}\dfrac{\partial(\mu d_{ij} u_i)}{\partial x_j} \end{cases} \tag{2.3.11}$$

The non-dimensional dynamical contribution of the stress tensor, d_{ij}, considering a Newtonian fluid and following the Stokes' hypothesis, is given by:

$$d_{ij} = 2\Big(S_{ij} - \frac{1}{3}S_{kk}\delta_{ij}\Big) \tag{2.3.12}$$

where S_{ij} is the non-dimensional strain rate tensor:

$$S_{ij} = \frac{1}{2}\Big(\frac{\partial u_i}{\partial x_j} + \frac{\partial u_j}{\partial x_i}\Big) \tag{2.3.13}$$

and the non-dimensional heat flux vector is

$$q_j = -\lambda \frac{\partial T}{\partial x_j} \tag{2.3.14}$$

The ideal gas law in non-dimensional form becomes

$$p = \rho R_0 T \tag{2.3.15}$$

The system is closed with laws that respectively define the non-dimensional total energy E and the non-dimensional viscosity $\mu(T)$, expressed by the non-dimensional Sutherland's law:

$$E = c_v \frac{p}{\rho} + \frac{1}{2}(u_i)^2 \tag{2.3.16}$$

$$\mu(T) = T^{\frac{3}{2}} \Big(\frac{1 + S/T_0}{T + S/T_0} \Big) \tag{2.3.17}$$

Since the non-dimensional groups γ,M_∞,Re and Pr are imposed, the reference variables may assume any value.
The most convenient choice is to assume $L_0 = 1, \rho_0 = 1$ and $T_0 = 1$ (so $R_0 = p_0/(\rho_0 T_0) = 1$) and to compute all the other parameters afterwards. Hence:

$$\gamma = \frac{c_{p0}}{c_{v0}} \qquad \text{heat specific ratio} \tag{2.3.18}$$

$$u_\infty = \sqrt{\gamma} M_\infty \qquad \text{free-stream velocity} \tag{2.3.19}$$

$$\mu_\infty = \frac{\sqrt{\gamma} M_\infty}{Re} \qquad \text{free-steam molecular viscosity} \tag{2.3.20}$$

$$k_\infty = \frac{c_{p0}}{Pr} \frac{\sqrt{\gamma} M_\infty}{Re} \qquad \text{free-stream thermal conductivity} \tag{2.3.21}$$

The governing equations for large eddy simulations are obtained by filtering equations (2.3.11) in order to separate the effects of the large-scale and small-scale motions.
Considering the case of spatially uniform filters (so, filtering operation and differentiation commute), we have:

$$\begin{cases} \dfrac{\partial \bar{\rho}}{\partial t} + \dfrac{\partial \overline{(\rho u_j)}}{\partial x_j} = 0 \\ \dfrac{\partial \overline{(\rho u_i)}}{\partial t} + \dfrac{\partial \overline{(\rho u_i u_j)}}{\partial x_j} = -\dfrac{\partial \bar{p}}{\partial x_i} + \dfrac{\sqrt{\gamma} M_\infty}{Re} \dfrac{\partial \overline{(\mu d_{ij})}}{\partial x_j} \\ \dfrac{\partial \overline{(\rho E)}}{\partial t} + \dfrac{\partial \overline{(\rho E u_j)}}{\partial x_j} = -\dfrac{\partial \overline{(p u_j)}}{\partial x_j} - \dfrac{c_p \sqrt{\gamma} M_\infty}{RePr} \dfrac{\partial \bar{q}_j}{\partial x_j} - \dfrac{\sqrt{\gamma} M_\infty}{Re} \dfrac{\partial \overline{(\mu d_{ij} u_i)}}{\partial x_j} \end{cases} \tag{2.3.22}$$

where

$$\bar{d}_{ij} = 2 \overline{\Big(S_{ij} - \frac{1}{3} S_{kk} \delta_{ij} \Big)} \tag{2.3.23}$$

and

$$\bar{q}_j = -\overline{\lambda \frac{\partial T}{\partial x_j}} \tag{2.3.24}$$

The equation of state becomes:

$$\bar{p} = R \overline{\rho T} \tag{2.3.25}$$

In the filtered Navier-Stokes equation there is one more unknown compared to the filtered incompressible Navier-Stokes equations, that is, the density $\bar{\rho}$.

This means that there is a triple product of unknown variables in the filtered convective terms (e.g., the SGS Reynolds stress becomes $\overline{\rho' u' v'}$).
An elegant way to simplify such equations is to apply the Favre filtering, that is defined as:

$$\tilde{f} = \frac{\overline{\rho \mathrm{f}}}{\bar{\rho}}$$

so $\overline{\rho f} = \bar{\rho}\tilde{f}$, where f is a general flow variable like velocity and temperature, but not density or pressure.
Hence, variables can be decomposed in two ways:

$$f = \bar{f} + f' \tag{2.3.26}$$

$$f = \tilde{f} + f'' \tag{2.3.27}$$

where $\bar{f}$ and $\tilde{f}$ are the resolved components and f' and f'' are the unresolved ones.

So the Favre filtered governing equations are:

$$\begin{cases} \dfrac{\partial \bar{\rho}}{\partial t} + \dfrac{\partial \bar{\rho}\tilde{u_j}}{\partial x_j} = 0 \\ \dfrac{\partial \bar{\rho}\tilde{u_i}}{\partial t} + \dfrac{\partial \bar{\rho}\tilde{u_i}\tilde{u_j}}{\partial x_j} = -\dfrac{\partial \bar{p}}{\partial x_i} + \dfrac{\sqrt{\gamma}M_\infty}{Re}\dfrac{\partial \bar{\mu}\bar{d}_{ij}}{\partial x_j} - \dfrac{\partial \bar{\tau}_{ij}^{SGS}}{\partial x_j} \\ \dfrac{\partial (\bar{\rho}\tilde{E})}{\partial t} + \dfrac{\partial [(\bar{\rho}\tilde{E} + \bar{p})\tilde{u_j}]}{\partial x_j} = -\dfrac{c_p\sqrt{\gamma}M_\infty}{RePr}\dfrac{\partial \tilde{q}_j}{\partial x_j} + \dfrac{\sqrt{\gamma}M_\infty}{Re}\dfrac{\partial (\bar{\mu}\bar{d}_{ij}\tilde{u}_i)}{\partial x_j} - \dfrac{\partial \bar{E}_j^{SGS}}{\partial x_j} \end{cases} \tag{2.3.28}$$

and the Favre-filtered equation of state is

$$\bar{p} = \bar{\rho} R_0 \tilde{T} \tag{2.3.29}$$

where the non-dimensional Favre-filtered strain rate tensor is:

$$\tilde{S}_{ij} = \frac{1}{2}\Big(\frac{\partial \tilde{u}_i}{\partial x_j} + \frac{\partial \tilde{u}_j}{\partial x_i}\Big) \tag{2.3.30}$$

the non-dimensional Favre-filtered heat flux vector is:

$$\tilde{q}_j = -\lambda \frac{\partial \tilde{T}}{\partial x_j} \tag{2.3.31}$$

and $\bar{\mu} = \mu(\tilde{T})$ is the non-dimensional molecular viscosity.

The effect of the small-scales motions is present in above equations through the subgrid scale stress tensor τ_{ij}^{SGS} in the Favre filtered momentum equation (2.3.28),

$$\bar{\tau}_{ij}^{SGS} = \overline{\rho u_i u_j} - \bar{\rho}\tilde{u}_i\tilde{u}_j \tag{2.3.32}$$

and the subgrid scale energy term $\bar{E}_j^{SGS}$ in the right-hand side of the filtered energy equation (2.3.28)

$$\bar{E}_j^{SGS} = \overline{(\rho E + p)u_i} - (\bar{\rho}\tilde{E} + \bar{p})\tilde{u}_i \tag{2.3.33}$$

$$\overline{\rho c_p T u_j} - \bar{\rho} c_p \tilde{T}\tilde{u_j} + \frac{1}{2}\bar{T}_{ij}^{SGS}\tilde{u_j} - \frac{1}{2}\bar{T}_{kk}^{SGS}\tilde{u_j} \tag{2.3.34}$$

As expected, equations (2.3.32) and (2.3.34) represent the unresolved turbulent contributions.
LES approach aims to model such terms in order to close the system of equations.

2.4 Modelling the SGS terms: WALE model and turbulent thermal conductivity

The quantity τ_{ij}^{SGS} in the momentum equation in (2.3.28) represents the effect of the subgrid-scale velocity component on the evolution of the large-scales motions.
Most of subgrid-scales models are based on the SGS turbulent eddy-viscosity assumption, μ_t^{SGS}, to model the subgrid-scales stress tensor [4].
Following the Boussinesq's hypothesis, the deviatoric part of the subgrid-scales stress tensor can be evaluated as:

$$\tau_{ij}^{SGS} - \frac{1}{3}\tau_{kk}^{SGS}\delta_{ij} = -2\mu_t^{SGS}\Big(\tilde{S}_{ij} - \frac{1}{3}\tilde{S}_{kk}\delta_{ij}\Big) \tag{2.4.1}$$

Similarly, the energy subgrid-scales terms are modelled through

$$\overline{\rho c_p T u_j} - \bar{\rho} c_p \tilde{T}\tilde{u_j} = -\lambda_t^{SGS}\frac{\partial \tilde{T}}{\partial x_j} \tag{2.4.2}$$

where λ_t^{SGS} is the subgrid-scales *turbulent diffusivity* [6] expressed by

$$\lambda_t^{SGS} = \mu_t^{SGS}\frac{c_p}{Pr_t} \tag{2.4.3}$$

Pr_t is the turbulent Prandtl number: it's assumed constant and equal to 0.9.

Starting from equations (2.4.2) and (2.4.3), the term $\bar{E}_j^{SGS}$ becomes:

$$\bar{E}_j^{SGS} = -\lambda_t^{SGS}\frac{\partial \tilde{T}}{\partial x_j} + \frac{1}{2}\bar{T}_{ij}^{SGS}\tilde{u_j} - \frac{1}{2}\bar{T}_{kk}^{SGS}\tilde{u_j} \tag{2.4.4}$$

Therefore, introducing equations (2.4.1) and (2.4.4) into the Favre-filtered Navier-Stokes equations and dropping the isotropic contribution of the subgrid-scales stress tensor results in the following non-dimensional set of conservative equations:

$$\begin{cases} \dfrac{\partial \bar{\rho}}{\partial t} + \dfrac{\partial \bar{\rho}\tilde{u_j}}{\partial x_j} = 0 \\ \dfrac{\partial \bar{\rho}\tilde{u_i}}{\partial t} + \dfrac{\partial \bar{\rho}\tilde{u_i}\tilde{u_j}}{\partial x_j} = -\dfrac{\partial \bar{p}}{\partial x_i} + \dfrac{\sqrt{\gamma}M_\infty}{Re}\dfrac{\partial(\bar{\mu}_{tot}\bar{d}_{ij})}{\partial x_j} \\ \dfrac{\partial(\bar{\rho}\tilde{E})}{\partial t} + \dfrac{\partial[(\bar{\rho}\tilde{E}+\bar{p})\tilde{u_j}]}{\partial x_j} = -\dfrac{\sqrt{\gamma}M_\infty}{Re}\bar{\lambda}_{tot}\dfrac{\partial \tilde{q}_j}{\partial x_j} + \dfrac{\sqrt{\gamma}M_\infty}{Re}\dfrac{\partial(\bar{\mu}_{tot}\bar{d}_{ij}\tilde{u}_i)}{\partial x_j} \end{cases} \tag{2.4.5}$$

where

$$\tilde{q}_j = -\lambda\frac{\partial \tilde{T}}{\partial x_j} \tag{2.4.6}$$

is the non-dimensional heat flux vector,

$$\bar{\mu}_{tot} = \mu(\tilde{T}) + \frac{Re}{\sqrt{\gamma}M_\infty}\mu_t^{SGS} \tag{2.4.7}$$

and

$$\bar{\lambda}_{tot} = c_p\Big(\frac{\mu(\tilde{T})}{Pr} + \frac{Re}{\sqrt{\gamma}M_\infty}\frac{\mu_t^{SGS}}{Pr_t}\Big) \tag{2.4.8}$$

denotes respectively the total dynamic viscosity (sum of the non-dimensional resolved molecular viscosity $\mu(\tilde{T})$ and the non-dimensional subgrid-scales viscosity) and the total diffusivity of the flow.

Hence, a suitable model for μ_t^{SGS} is required to close the system.

In Smagorinsky's model [21, 4], the turbulent eddy viscosity is assumed to be proportional to the subgrid characteristic length Δ (expressing the size of the filter) and to a characteristic turbulent velocity taken as the local strain rate $|\tilde{S}|$ multiplied by Δ:

$$\mu_{sgs} = \bar{\rho}(C_s\Delta)^2|\tilde{S}| \tag{2.4.9}$$

where $|\tilde{S}| = \sqrt{2\tilde{S}_{ij}\tilde{S}_{ij}}$ and C_s is the Smagorinsky's constant (in general, $C_s \approx 0.18$ [6]).
However, this model gives a non-zero value of μ_t^{SGS} as long as the velocity gradient exists, so near a wall all turbulent fluctuations should be damped to get the correct condition.

To this end, the Van Driest [39] exponential damping function $1 - e^{-\frac{y^+}{A^+}}$, with $A^+ = 25$ (where y^+ is the wall distance express in Kolmogorov units), was widely used in early LES studies.
Nevertheless, it produces an asymptotic behaviour in the near wall-regions equal to $\mu_{SGS} \sim O(y^+)^2$, that is not physically consistent to the wall-turbulence theory, which predicts a behaviour equal to $\mu_{SGS} \sim O(y^+)^3$ in the inner layer.
An elegant solution to solve the near-wall region problem on fine grids is to use a combination of resolved velocity spatial derivatives that exhibits the expected asymptotic behaviour $\mu_t^{SGS} \sim O(y^+)^3$. The method, known as *Wall-Adapting Local Eddy-Viscosity Model (WALE)*, defines the SGS turbulent eddy viscosity [10] as:

$$\mu_t^{SGS} = \bar{\rho}\Delta^2 C_w^2 \frac{(\tilde{S}_{ij}^d\tilde{S}_{ij}^d)^3/2}{(\tilde{S}_{ij}\tilde{S}_{ij})^5/2 + (\tilde{S}_{ij}^d\tilde{S}_{ij}^d)^5/4} \tag{2.4.10}$$

where $C_w \approx \sqrt{10.6}C_s$ is a constant, and

$$\tilde{S}_{ij}^d = \frac{1}{2}\Big(\frac{\partial\tilde{u}_i}{\partial x_l}\frac{\partial\tilde{u}_l}{\partial x_j} + \frac{\partial\tilde{u}_j}{\partial x_l}\frac{\partial\tilde{u}_l}{\partial x_i}\Big) + \frac{1}{3}\frac{\partial\tilde{u}_m}{\partial x_l}\frac{\partial\tilde{u}_l}{\partial x_m}\delta_{ij} \tag{2.4.11}$$

is the traceless symmetric part of the square of the resolved velocity gradient tensor.
This model possesses also the interesting property that the subgrid viscosity vanishes when the flow is two-dimensional, in agreement with the physical analysis [10].

Chapter 3

Dynamics of boundary layer

3.1 Boundary layer fundamentals

Generally, the motion field determination around any objects or into a channel can be obtained by resolving the mass, momentum and energy conservation equations (i.e., the Navier-Stokes equations). However, such an approach has some difficulties, that can be overcome by simplifying the governing equations adopting the concept of *boundary layer*, still guaranteeing the physics of the phenomenon. According to Prandtl's boundary layer theory, in flows with high Reynolds number, *Re*, two different regions can be distinguished: the first one, in which viscous and heat effects can be neglected, so the motion field is governed by Euler's equations with good approximation; the second one, usually very thin (boundary layers and wakes), in which high flux gradients (in wall-normal direction) and viscous effects are relevant.

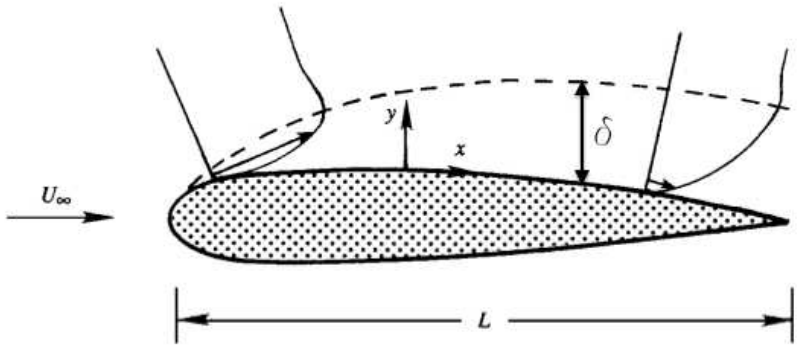

Figure 3.1: Boundary layer on an airfoil [26]

Here, assuming steady wall with no-slip condition, the velocity increases from zero at the wall itself (tangential components-adherence conditions- and normal component-impermeability condition) to the value at the edge of the boundary layer, imposed by the external solution.

Starting from figure (3.2), concerning the simplest wall flow (i.e., a flow on a flat plate), it's worth noting that the boundary layer thickness, δ, grows up along the streamwise direction, x, due to the bigger portion of fluid characterised by viscous effects.

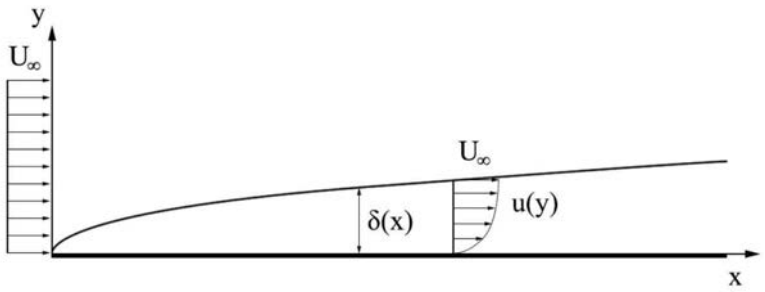

Figure 3.2: Boundary layer of an incompressible flow on a flat plate [37]

There are several formal definitions of the boundary layer thickness in literature.
The most intuitive is the δ_{99}, according to which the boundary layer thickness is that normal distance from the wall to which the streamwise velocity is equal to 99 % of the undisturbed one.
Another important definition is the *displacement thickness* δ^*, that evaluates the mass defect compared to the non-viscous flux due to the boundary layer existence. So, it represents the distance to which the external solution should be moved to get the same mass flux of the real solution through the boundary layer.

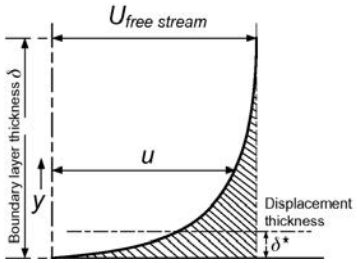

Figure 3.3: Graphic representation of the displacement thickness concept [20]

Mathematically, the definition of δ^* is:

$$\delta^* = \int_0^h 1 - \frac{u}{u_{e,0}} dy \tag{3.1.1}$$

where:

- h is a distance from the wall far enough to be out of the boundary layer
- $u_{e,0}$ is the velocity of the external solution

It's important to notice that this interpretation is valid only under incompressible assumptions, while for compressible flows it's necessary to consider the density variations into the boundary layer.

Regarding the flat plate described in figure 3.2, the boundary layer thickness $\delta(x)$ can be expressed as a function of the streamwise coordinate x with respect to the leading edge of the plate. [37]
It's convenient to subdivide the domain into three different regions along the x direction, according to the Reynolds number [1], which for the case of the flat plate can be defined as:

$$Re_x = \frac{U_\infty}{\nu} x \tag{3.1.2}$$

[1] that increases too along the x direction

where U_∞ is the velocity of the free stream, ν the kinematic viscosity.
If $Re_x < 10$, the boundary layer is not formed yet, because the viscous effects are comparable with the inertial ones ($Re_x \sim 1$), so there isn't the separation of regions described previously.

If $10^2 < Re_x < 10^4$ the boundary layer has a laminar nature.

Into this range, at a sufficiently large distance from the leading edge ($10^3 < Re_x < 10^4$), where the solution does not depend on the initial condition (similarity region), it can be obtained that, under the hypothesis of:

- semi-infinite flat plate
- incompressible flow
- stationarity
- bi-dimensional problem

the boundary layer thickness respects the following law:

$$\delta(x) = \frac{\alpha}{\sqrt{Re_x}} x \tag{3.1.3}$$

where α is a parameter that depends on the model assumed to describe the velocity profile $u(y)$.

In the case of the *Blasius solution* we have that $\alpha \approx 4.9$.
Substituting in (3.1.3) we obtain:

$$\delta(x) = \frac{4.9}{\sqrt{Re_x}} x = \frac{4.9}{\sqrt{\frac{\rho U_\infty x}{\mu}}} x = 4.9\sqrt{\frac{\nu x}{U_\infty}} \tag{3.1.4}$$

in which it's explicated the dependence on x of the boundary layer thickness.

If $Re_x > 10^4$ the motion becomes gradually more and more irregular until, when $Re_x \gtrsim 10^6$, the boundary layer is completely turbulent.
Hence, it consists of several eddies with different dimensions, with a tri-dimensional and non-stationary behaviour. So, it is no longer possible to describe the flow as in the laminar assumption.

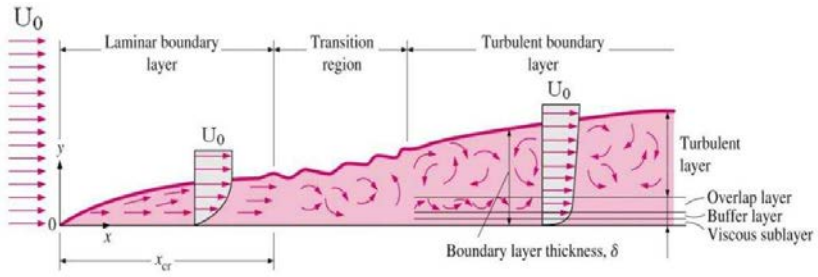

Figure 3.4: Development of the kinematic boundary layer on a flat plate [25]

Concerning the thermal field solution and the thermal flux between an object and the surrounding flow, similar considerations can be done.
Let's consider a body immersed in a fluid with a lower temperature than the body itself.
If the fluid is at rest, the temperature field is evenly distributed in all directions: we have a thermal flux from the body to the fluid thanks only to the thermal conductivity.

If the fluid is in motion, the flow carries the internal energy of the undisturbed flow towards the body: so, the temperature field depends on the balance between the convective and diffusive thermal flows. In particular, the region that is influenced by the temperature of the body is reduced to a single layer next to the wall and to the wake behind the body itself. [1]

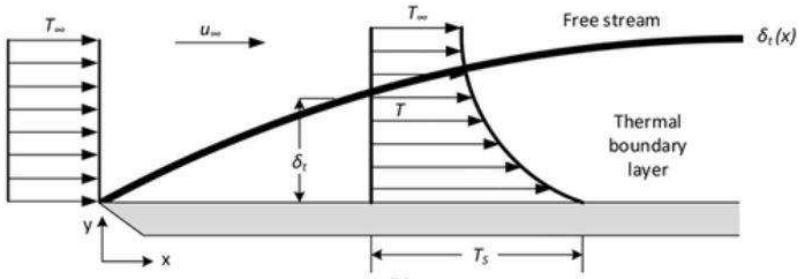

Figure 3.5: Thermal boundary layer on a flat plate [35]

This layer, called *thermal boundary layer*, is as thinner as higher is the velocity, and it can be defined as the region in which diffusive terms are comparable to convective ones.
As in the kinematic boundary layer case, the small thermal boundary layer thickness derives from the fact that most of interesting fluids (liquids and gasses) has very low thermal conductivity.
By evaluating the conductive term as $q = -\lambda(T_\infty - T_w)/\delta_T$, it's reasonable that its flux in wall normal direction can be high and so comparable to the convective one only if δ_T is very small.
As the fluid dynamics field, the temperature field can be subdivided into two regions: the first one, the external field, in which the thermal flux is due only to the convective term, while the conduction one in negligible; the second one, the thermal boundary layer, in which conductive terms are not negligible (see figure 3.5).

3.2 Kinematic and thermal fields coupling

The incompressible boundary layer can be described by the *boundary layer equations* (see appendix A).
It's worth noting that, in general, the solutions of kinematic and temperature fields are not independent: indeed, it's necessary to know the velocity field in order to determine the convective thermal flux (and so, the temperature field).
However, while in the incompressible case the kinematic field solution does not depend on the thermal field (indeed, the temperature is a passive scalar), in flows in which the compressibility and the variation of temperature are not negligible, the analysis should be carried out keeping into account also the variations of ρ and T, using the energy equation: consequently, kinematic and thermal fields are coupled.

The so-called thermal energy equation can be written in the shape (see appendix B):

$$\rho\frac{De}{Dt} = -\nabla\cdot\mathbf{q} - p\nabla\cdot\mathbf{v} + \tau : \nabla\mathbf{v} \tag{3.2.1}$$

where e is the internal energy.

Such equation permits to evaluate the temperature variations due to heat transfer by conduction ($\nabla\cdot\mathbf{q}$), to reversible compression ($p\nabla\cdot\mathbf{v}$) and to irreversible viscous dissipation $\tau : \nabla\mathbf{v}$.
The last two terms represent the conversion of mechanical energy into thermal energy.
For a Newtonian fluid, the viscous dissipation term can be written as:

$$\tau : \nabla \mathbf{v} = \mu \Phi_v \tag{3.2.2}$$

where Φ_v is the *viscous dissipation function*.

Thanks to the mass conservation equation, we obtain:

$$\nabla \cdot \mathbf{v} = -\frac{1}{\rho}\frac{D\rho}{Dt} \tag{3.2.3}$$

Remembering that, under perfect gas hypothesis

$$dh = de + d\Big(\frac{p}{\rho}\Big) \longrightarrow c_p dT = c_v dT + d\Big(\frac{1}{\rho}\Big) \tag{3.2.4}$$

the equation (3.2.1) becomes:

$$\rho c_p \frac{DT}{Dt} = \nabla \cdot (\lambda \nabla T) + \frac{Dp}{Dt} + \mu \Phi_v \tag{3.2.5}$$

Starting from (3.2.5), it's convenient to carry out a dimensional analysis.
Let's consider the Navier-Stokes equations.
By assuming that the molecular viscosity μ, the thermal conductivity λ and the viscous coefficient Λ are constant, we have:

$$\begin{cases} \dfrac{D\rho}{Dt} + \rho \nabla \cdot \mathbf{v} = 0 \\ \rho \dfrac{D\mathbf{v}}{Dt} + \nabla p = \mu \nabla^2 \mathbf{v} + (\Lambda + \mu) \nabla (\nabla \cdot \mathbf{v}) + \rho \mathbf{g} \\ \rho c_p \dfrac{DT}{Dt} = \nabla \cdot (\lambda \nabla T) + \dfrac{Dp}{Dt} + \mu \Phi_v \end{cases} \tag{3.2.6}$$

In hydrostatic equilibrium conditions (**v** = 0), the momentum conservation equation in equations (3.2.6) becomes:

$$\nabla p_s = \rho_\infty \mathbf{g} \tag{3.2.7}$$

where p_s is the hydrostatic pressure.

By subtracting the (3.2.7) from the momentum conservation equation in equations (3.2.6), we have:

$$\rho \frac{D\mathbf{v}}{Dt} + \nabla p' = \mu \nabla^2 \mathbf{v} + (\Lambda + \mu) \nabla (\nabla \cdot \mathbf{v}) + (\rho - \rho_\infty) \mathbf{g} \tag{3.2.8}$$

where p' is the difference between the static pressure and the hydrostatic pressure p_s.

Let us introduce the non-dimensional variables:

$$x^* = \frac{x}{L_0}, \quad t^* = \frac{U_\infty}{L_0} t, \quad \mathbf{v}^* = \frac{\mathbf{v}}{U_\infty}, \quad \rho^* = \frac{\rho}{\rho_\infty}, \quad p^* = \frac{p'}{\rho_\infty U_\infty^2}, \quad T^* = \frac{T}{\Delta T_0} \tag{3.2.9}$$

where L_0 is a characteristic dimension of the body and $\Delta T_0 = T_w - T_\infty$, with T_w the temperature of the body.

By substituting these variables in (3.2.6), using equation (3.2.8) in place of the momentum conservation equation, and omitting the symbol $'*'$ in order to get a smoother reading, we have:

$$\begin{cases} \dfrac{D\rho}{Dt} + \rho\nabla\cdot\mathbf{v} = 0 \\ \rho\dfrac{D\mathbf{v}}{Dt} + \nabla p = \dfrac{1}{Re}\Big[\nabla^2\mathbf{v} + \Big(1+\dfrac{\Lambda}{\mu}\Big)\nabla(\nabla\cdot\mathbf{v})\Big] + \dfrac{1}{Fr^2}(\rho-1)\mathbf{j} \\ \rho\dfrac{DT}{Dt} = \dfrac{1}{PrRe}\nabla^2 T + E\dfrac{Dp}{Dt} + \dfrac{E}{Re}\Phi_v \end{cases} \tag{3.2.10}$$

where **j** is the unit vector along the direction of the gravitational force, and the non-dimensional numbers are defined as:

$$Re = \frac{U_\infty L_0}{\nu} \qquad \text{Reynolds number}$$
$$Fr = \frac{U_\infty}{\sqrt{gL_0}} \qquad \text{Froude number}$$
$$Pr = \frac{\mu c_p}{\lambda} \qquad \text{Prandtl number}$$
$$E = \frac{U_\infty^2}{c_p \Delta T_0} \qquad \text{Eckert number}$$

In particular, the Reynolds number represents the ratio between inertial and viscous forces, the Froude number the one between inertial and gravitational forces.
Prandtl number is a characteristic of the fluid itself, and it represents the ratio between the momentum diffusivity and the thermal diffusivity.
The Eckert number can be expressed as the ratio between two characteristic temperature differences. Indeed, remembering that the stagnation temperature can be defined as $T^0 = T + \frac{v^2}{2c_p}$, we have:

$$\frac{U_\infty^2}{c_p} = 2(T_\infty^0 - T_\infty) = 2\Delta T_a \tag{3.2.11}$$

where ΔT_a is the temperature increment in an adiabatic compression.
Hence, the Eckert number can be expressed as:

$$E = 2\frac{\Delta T_a}{\Delta T_0} \tag{3.2.12}$$

Starting from these results, three cases can be observed.

- $M_\infty < 0.3$, that is, flows with low velocity (with $U_\infty \lesssim 100$ m/s)
  In this case, the dependence of the density from pressure and temperature can be considered negligible.
  The Froude number is high, so the gravitational term is negligible, and the Eckert number is sufficiently small ($\Delta T_a \simeq 5K$ if $U_\infty = 100m/s$).
  Therefore, the dissipation and compression terms can be neglected.
  Equations (3.2.10) result:

$$\begin{cases} \nabla\cdot\mathbf{v} = 0 \\ \dfrac{D\mathbf{v}}{Dt} + \nabla p = \dfrac{1}{Re}\nabla^2\mathbf{v} \\ \dfrac{DT}{Dt} = \dfrac{1}{PrRe}\nabla^2 T \end{cases} \tag{3.2.13}$$

  It's worth noting that the mass and the momentum conservation equations are independent of the temperature, so the kinematic field can be resolved regardless of the thermal one.

- $0.3 < M_\infty < 1$, that is, flows with intermediate velocity
  In this case, the incompressible hypothesis is not valid, but the dependence of density on temperature is still negligible.
  The Eckert number is of order 1, so the compression term can't be neglected, but the dissipation term, that is divided by $Re \gg 1$, is negligible.
  Thus, the equations result:

$$\begin{cases} \dfrac{D\rho}{Dt} + \rho\nabla\cdot\mathbf{v} = 0 \\ \rho\dfrac{D\mathbf{v}}{Dt} + \nabla p = \dfrac{1}{Re}\Big[\nabla^2\mathbf{v} + \Big(1+\dfrac{\Lambda}{\mu}\Big)\nabla(\nabla\cdot\mathbf{v})\Big] \\ \rho\dfrac{DT}{Dt} = \dfrac{1}{PrRe}\nabla^2 T + E\dfrac{Dp}{Dt} \end{cases} \tag{3.2.14}$$

  Even in this case the kinematic field does not depend on the thermal one.

- $M_\infty > 1$, that is, flows at high velocity
  The Froude number is sufficiently high, so the gravitational term can be neglected.
  The higher the M_∞ value, the higher the value of ΔT_a, so the temperature variations into the field are so large that the relative density variations can't be neglected.
  Moreover, molecular viscosity and thermal conductivity can't be considered constant on temperature.
  So, the kinematic field is coupled with the thermal one and the system, consisting of equations (3.2.10) with the state law and laws of $\mu(T)$ and $\lambda(T)$, must be solved simultaneously.

3.3 Compressible boundary layer equations

Under the hypothesis of bi-dimensional and stationary flow, not keeping into account the variability of μ and λ, remembering that the kinematic and the thermal boundary layer thicknesses are small compared to the characteristic dimension of the body L_0, the equation of energy in equations (3.2.10) becomes:

$$\begin{matrix} \rho\Big(u\dfrac{\partial T}{\partial x} + v\dfrac{\partial T}{\partial y}\Big) = \dfrac{1}{Pr}\dfrac{1}{Re}\Big(\dfrac{\partial^2 T}{\partial x^2} + \dfrac{\partial^2 T}{\partial y^2}\Big) + E\Big(u\dfrac{\partial p}{\partial x} + v\dfrac{\partial p}{\partial y}\Big) + E\dfrac{1}{Re}\Phi_v \\ 1\cdot 1 \quad \delta\cdot\dfrac{1}{\delta_T} \qquad\qquad \delta^2 \quad 1 \quad \dfrac{1}{\delta_T^2} \qquad\qquad 1\cdot 1 \quad \delta\cdot\delta \qquad \delta^2\cdot\dfrac{1}{\delta^2} \end{matrix} \tag{3.3.1}$$

with:

$$\delta \ll 1 \qquad , \qquad \delta_T \ll 1 \tag{3.3.2}$$

where δ_T is the non-dimensional thickness of the thermal boundary layer, δ the non-dimensional kinematic boundary layer thickness (both of them with reference to the characteristic length of the body L_0).

It's worth noting that Pr is of order 1 for gasses (about 0.7 for air) and between 10 and 1000 for liquids.
From the incompressible analysis (see appendix A), we have:

$$\begin{cases} v \sim \delta & \\ \dfrac{\partial p}{\partial y} \sim \delta & \\ Re \sim \dfrac{1}{\delta^2} & \\ y \sim \delta & \text{into the boundary layer} \\ y \sim \delta_T & \text{into the thermal boundary layer} \end{cases}$$

thus, relying on information given by equations, (3.3.1) we can deduct that for $Re \to \infty$:

$$\frac{\partial^2 T}{\partial x^2} / \frac{\partial^2 T}{\partial y^2} \to 0$$
$$v\frac{\partial p}{\partial y} / u\frac{\partial p}{\partial x} \to 0$$

The non-dimensional dissipation function Φ_v consists of the sum of the different squared derivatives of the velocity components. So, basing on equations (3.3.3), only the term $(\partial u/\partial y)^2$ is relevant, and it scales with $1/\delta^2$.

The compression and dissipative terms are comparable only if the Eckert number is of order 1.
Since the conductive and the convective terms must be comparable into the thermal boundary layer, if $\delta/\delta_T \ll 1$ the most important convective term is the x one.
There will be:

$$\left(\frac{\delta}{\delta_T}\right)^2 \frac{1}{Pr} \sim 1 \tag{3.3.3}$$

This means that:

$$\frac{\delta}{\delta_T} \sim \sqrt{Pr} \tag{3.3.4}$$

from which it's possible to have a good estimate of the ratio between the kinematic and the thermal boundary layer thicknesses.
The (3.3.4) is valid only if $Pr \ll 1$, so for liquid metals.
If $\delta/\delta_T \gg 1$, the most important convective term is the y one:

$$\left(\frac{\delta}{\delta_T}\right)^2 \frac{1}{Pr} \sim \frac{\delta}{\delta_T} \tag{3.3.5}$$

from which:

$$\frac{\delta}{\delta_T} \sim Pr \tag{3.3.6}$$

that is valid for liquids.
In the case of gasses, for which $Pr \simeq 1$, the two thicknesses have the same order of magnitude, so both the convective terms are important.
In this way the boundary layer equations, under bi-dimensional, compressible and stationary flow hypothesis, can be written as (in dimensional form):

$$\begin{cases} \dfrac{\partial(\rho u)}{\partial x} + \dfrac{\partial(\rho v)}{\partial y} = 0 \\ \rho\Big(u\dfrac{\partial u}{\partial x} + v\dfrac{\partial u}{\partial y}\Big) = -\dfrac{dp}{dx} + \dfrac{\partial}{\partial y}\Big(\mu\dfrac{\partial u}{\partial y}\Big) \\ \rho c_p\Big(u\dfrac{\partial T}{\partial x} + v\dfrac{\partial T}{\partial y}\Big) = u\dfrac{dp}{dx} + \dfrac{\partial}{\partial y}\Big(\lambda\dfrac{\partial T}{\partial y}\Big) + \mu\Big(\dfrac{\partial u}{\partial y}\Big)^2 \end{cases} \tag{3.3.7}$$

with the following boundary conditions:

- y = 0 $\longrightarrow$ $u = v = 0$ $T = T_w$ $\rho = \rho_w$
- y = δ $\longrightarrow$ $u \to U_e(x)$ $T \to T_e(x)$ $\rho \to \rho_e(x)$

where also the variation of μ and λ is considered, while the specific heat is assumed constant.
The subscript 'e' denotes quantities evaluated at the edge of the boundary layer.
It's important to notice that the pressure is not unknown thanks to the solution of the external field, and it varies only in the x direction, since into the boundary layer $\partial p/\partial y = 0$.

Equations (3.3.7), together with the state law and the laws of $\lambda(T)$ and $\mu(T)$, defined a system of 6 equations in the variables $u, v, \rho, T, \lambda, \mu$.
In the case of air, Sutherland's law provides good results for μ.

It's worth noting that, in the case of incompressible flow and constant properties, the energy conservation equation in (3.3.7) becomes:

$$\rho c_p\Big(u\frac{\partial T}{\partial x} + v\frac{\partial T}{\partial y}\Big) = \lambda\frac{\partial^2 T}{\partial y^2} + \mu\Big(\frac{\partial u}{\partial y}\Big)^2 \tag{3.3.8}$$

In this case, the temperature is independent of velocity, so only equations from mass and momentum conservation can be resolved, while the temperature field can be found afterwards.

The boundary layer equations obtained previously are valid only for compressible *laminar* flow.

In the case of turbulent compressible flow, it's convenient to introduce the decomposition of the different quantities in mean and fluctuation parts, including density and temperature.

By imposing the Reynolds' average operator to the boundary layer equations of compressible flows, the following equations are obtained, valid for turbulent boundary layer:

$$\begin{cases} \dfrac{\partial(\overline{\rho u})}{\partial x} + \dfrac{\partial(\overline{\rho v})}{\partial y} = 0 \\ \overline{\rho u}\dfrac{\partial \bar{u}}{\partial x} + \overline{\rho v}\dfrac{\partial \bar{u}}{\partial y} = -\dfrac{d\bar{p}}{dx} + \dfrac{\partial \tau}{\partial y} \\ \overline{\rho u} c_p\dfrac{\partial \bar{T}}{\partial x} + \overline{\rho v} c_p\dfrac{\partial \bar{T}}{\partial y} = \bar{u}\dfrac{d\bar{p}}{dx} + \dfrac{\partial q}{\partial y} + \tau\dfrac{\partial \bar{u}}{\partial y} \end{cases} \tag{3.3.9}$$

where:

$$\tau = \bar{\mu}\frac{\partial \bar{u}}{\partial y} - \overline{\rho u' v'} \tag{3.3.10}$$

$$q = \bar{\lambda}\frac{\partial \bar{T}}{\partial y} - \overline{\rho v' h'} \tag{3.3.11}$$

Assuming the following definitions in order to model the triple correlation terms:

$$-\overline{\rho u' v'} = \mu_t \frac{\partial \bar{u}}{\partial y} \tag{3.3.12}$$

$$-\overline{\rho v' h'} = \lambda_t \frac{\partial \bar{T}}{\partial y} \tag{3.3.13}$$

where μ_t is the turbulent eddy viscosity and λ_t is the turbulent eddy conductivity, we can rewrite the compressible turbulent boundary layer equations as:

$$\begin{cases} \dfrac{\partial(\overline{\rho u})}{\partial x} + \dfrac{\partial(\overline{\rho v})}{\partial y} = 0 \\ \overline{\rho u}\dfrac{\partial \bar{u}}{\partial x} + \overline{\rho v}\dfrac{\partial \bar{u}}{\partial y} = -\dfrac{d\bar{p}}{dx} + \dfrac{\partial}{\partial y}\Big[(\mu + \mu_t)\dfrac{\partial \bar{u}}{\partial y}\Big] \\ \overline{\rho u} c_p \dfrac{\partial \bar{T}}{\partial x} + \overline{\rho v} c_p \dfrac{\partial \bar{T}}{\partial y} = \bar{u}\dfrac{d\bar{p}}{dx} + \dfrac{\partial}{\partial y}\Big[(\lambda + \lambda_t)\dfrac{\partial \bar{T}}{\partial y}\Big] + (\mu + \mu_t)\Big(\dfrac{\partial u}{\partial y}\Big)^2 \end{cases} \tag{3.3.14}$$

where for the heat transfer, in analogy with turbulent stress, we have:

$$q_l = -\lambda \frac{\partial \bar{T}}{\partial y} \qquad \text{laminar heat flow} \tag{3.3.15}$$

$$q_T = -\lambda_t \frac{\partial \bar{T}}{\partial y} \qquad \text{turbulent heat flow} \tag{3.3.16}$$

and λ_t can be determined basing on the turbulent Prandtl number:

$$Pr_t = \frac{\mu_t c_p}{\lambda_t} \tag{3.3.17}$$

where Pr_t is about 1 ($Pr_t \simeq 0.7$).
The typical first step to analyse such equations is to eliminate $\overline{\rho v}$ from the momentum and energy equations by means of the continuity relation, leaving only two equations in three variables $\bar{\rho}$,$\bar{u}$,$\bar{T}$.
Another relation is necessary to close the system, which is the state equation of the fluid.
Under the perfect gas approximation, we have $\bar{p} = \bar{\rho} R \bar{T}$.
It's worth noting that, to obtain such equations, also the approximation $d\bar{h} = c_p d\bar{T}$ has been done.
Since $\bar{p}$ is nearly constant through the boundary layer, the density profile is directly related to the temperature profile by the perfect gas law:

$$\frac{\bar{\rho}(y)}{\rho_\infty} = \frac{T_\infty}{\bar{T}(y)} \tag{3.3.18}$$

which simplifies greatly the algebra.
The boundary conditions are:

- y = 0 $\longrightarrow$ $\bar{u} = \overline{uv} = 0$; $\bar{T} = T_w$ $\bar{\rho} = \rho_w$
- y = δ $\longrightarrow$ $\bar{u} \to U_e(x)$; $\bar{T} \to T_e(x)$ $\bar{\rho} \to \rho_e(x)$

If the turbulent shear stress and heat flux are properly correlated, these equations and boundary conditions are well defined and solvable in parabolic matching style, like their laminar counterparts.

Chapter 4

Solver considerations

The present work has been carried out with Unsteady Robust All-around Navier-StOkes Solver (URANOS) by Francesco De Vanna's PhD activity [9, 8], a numerical solver for compressible viscous flows, capable of dealing with moving bodies at high Mach numbers with high order accuracy and high resolution.
The governing system consists of the LES Favre-filtered equations, that are obtained in section 2.3. Such system is closed considering the Favre-filtered state equation of the fluid, the Favre-filtered definition of total energy and the Sutherland's law for the molecular viscosity.
Moreover, the subgrid-scale terms are modelled as in section 2.4, using the concepts of SGS turbulent eddy viscosity μ_t^{SGS} and SGS turbulent eddy diffusivity λ_t^{SGS}.
All these equations are summarised below.

$$\begin{cases} \dfrac{\partial \bar{\rho}}{\partial t} + \dfrac{\partial \bar{\rho}\tilde{u_j}}{\partial x_j} = 0 \\ \dfrac{\partial \bar{\rho}\tilde{u_i}}{\partial t} + \dfrac{\partial \bar{\rho}\tilde{u_i}\tilde{u_j}}{\partial x_j} = -\dfrac{\partial \bar{p}}{\partial x_i} + \dfrac{\sqrt{\gamma}M_\infty}{Re}\dfrac{\partial(\bar{\mu}_{tot}\bar{d}_{ij})}{\partial x_j} \\ \dfrac{\partial(\bar{\rho}\tilde{E})}{\partial t} + \dfrac{\partial[(\bar{\rho}\tilde{E}+\bar{p})\tilde{u_j}]}{\partial x_j} = -\dfrac{\sqrt{\gamma}M_\infty}{Re}\bar{\lambda}_{tot}\dfrac{\partial \tilde{q}_j}{\partial x_j} + \dfrac{\sqrt{\gamma}M_\infty}{Re}\dfrac{\partial(\bar{\mu}_{tot}\bar{d}_{ij}\tilde{u}_i)}{\partial x_j} \\ \bar{p} = \bar{\rho}R_0\tilde{T} \\ \tilde{E} = c_v\dfrac{\bar{p}}{\bar{\rho}} + \dfrac{1}{2}\tilde{u_i}\tilde{u_i} \end{cases} \tag{4.0.1}$$

where

$$\bar{d}_{ij} = 2\Big(\tilde{S}_{ij} - \frac{1}{3}\tilde{S}_{kk}\delta_{ij}\Big) \tag{4.0.2}$$

is the dynamical term of the non-dimensional stress tensor,

$$\tilde{S}_{ij} = \frac{1}{2}\Big(\frac{\partial \tilde{u}_i}{\partial x_j} + \frac{\partial \tilde{u}_j}{\partial x_i}\Big) \tag{4.0.3}$$

is non-dimensional Favre-filtered strain rate tensor,

$$\tilde{q}_j = -\lambda\frac{\partial \tilde{T}}{\partial x_j} \tag{4.0.4}$$

is the non-dimensional Favre-filtered heat flux vector,

$$\bar{\mu}_{tot} = \mu(\tilde{T}) + \frac{Re}{\sqrt{\gamma}M}\mu_t^{SGS} \tag{4.0.5}$$

and

$$\bar{\lambda}_{tot} = c_p\Big(\frac{\mu(\tilde{T})}{Pr} + \frac{Re}{\sqrt{\gamma}M}\frac{\mu_t^{SGS}}{Pr_t}\Big) \tag{4.0.6}$$

denotes the total dynamic viscosity (sum of the non-dimensional resolved molecular viscosity $\mu(\tilde{T})$ and the non-dimensional subgrid-scale viscosity) and the total diffusivity of the flow respectively.
The molecular viscosity $\mu(\tilde{T})$ depends on the temperature for Newtonian fluids, since it is strictly related to molecular interactions.
The kinetic theory of Sutherland provides the well-known *Sutherland's law* [37], that is used in this work:

$$\mu(\tilde{T}) = \Big(\frac{S + T_0'}{S + \tilde{T}}\Big)\tilde{T}^{\frac{3}{2}} \tag{4.0.7}$$

where T_0' is the reference value of 273.15 K and S is the constant *effective temperature*, that depends on the fluid: in this analysis only air is involved, so S = 110.4.
The turbulent Prandtl number Pr_t is set constant and equal to 0.9.
Analyses along streamwise and spanwise directions have been carried out with a *wall-resolved* approach through implicit LES (ILES), so no model is assumed to describe the subgrid-scale terms.
This means that formally unresolved DNSs have been used for such simulations, because SGS terms are neglected.
Analyses along wall-normal direction have been carried out with a *wall-modelling* approach, solving the Favre-filtered Navier-Stokes equations whose SGS terms are modelled according to the Wall-Adapting Local Eddy-Viscosity Model (WALE, see section 2.4).
Such simulations have been tested with two different wall-models, that are described in chapter 6.
It's worth noting that in every simulation the filter spacing is imposed by the computational grid resolution, in particular $\Delta = (\Delta x \Delta y \Delta z)^{\frac{1}{3}}$.

We'd like to emphasise that the governing equations are in non-dimensional formulation to carry out the computation, and the reference variables are imposed unitary (see section 2.3).
The non-dimensional group values used for the simulations are summarised below:

$\gamma = 1.4$	heat capacity ratio
$M_\infty = 2$	free-stream Mach number
$Re = 8346$	Reynolds number
$Pr = 0.71$	Prandtl number

The friction Reynolds number [1] at the inflow is instead $Re_\tau = 180$.

[1] an important parameter that quantifies the turbulence intensity; more in detail, it evaluates the separation between large scales and small scales

Chapter 5

Spatial discretization of the domain

5.1 Grid requirements

The grid used to generate the fluid-domain's discretization is three-dimensional, as requested for a LES analysis.
In particular, the system is described with reference to a ground left-handed frame, that is oriented in order to have the y-axis aligned with the wall-normal direction, the x-axis with the streamwise direction and the z-axis with the spanwise direction (see figure 1.1).

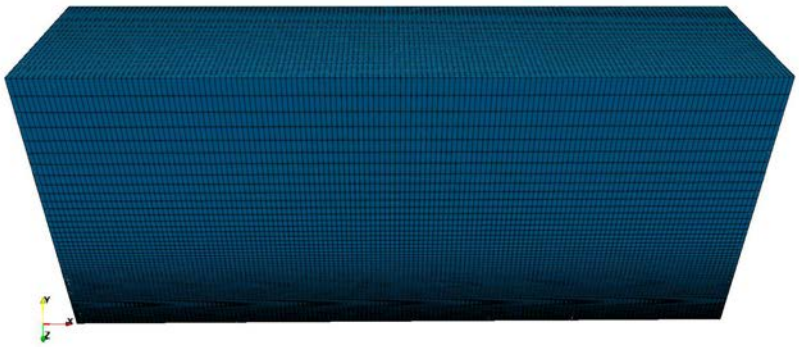

Figure 5.1: Computational grid representation

As the reader can see from Figure 1.1, the grid is uniform along the x-axis, with a number of nodes high enough to reach accurate results, but still considering the computational cost.
Usually for a good LES, in the viscous sublayer a reasonable value of Δx^+ between 20 and 40 is requested [18].
The discretization along the z-axis is similar: in this case, the value of Δz^+ derives from the necessity of catching the physical phenomenon related to the streaks, that is, coherent vortical structures in the boundary layer that are responsible for the turbulent kinetic energy production.
Observing the system along a plane on a given wall coordinate y^+, such vortices outline some alternating stripes with high and low velocities, whose mean span size is about 25 viscous units.
Hence, a value of Δz^+ between 10 and 20 is high enough to describe the process of the turbulent production, and so the correct dynamics of the problem.
The grid along the y-axis is different from the other cases.
Because of the strong variations of the physical quantities which describe the fluid domain into the boundary layer, a high number of nodes is required for a wall-resolved boundary layer approach.
The grid resolution along this direction should be characterised by a value of Δy^+ of about 1 at the

wall, with a hyperbolic distribution, so the density of nodes decreases moving away from the wall itself.
This permits to get a gain in terms of computational cost, still guaranteeing a good resolution.

It's interesting to compare what the grid requirements are for a good DNS

- $\Delta x^+ \approx 10$
- $\Delta y^+ \approx 1$
- $\Delta z^+ \approx 5$

with those ones associated to the LES approach:

- $\Delta x^+ \approx 20 \div 40$
- $\Delta y^+ \approx 1$
- $\Delta z^+ \approx 10 \div 20$

Hence, the latter permits to significantly decrease the simulation time.

5.2 Analyses of the domain size along spanwise direction

The first aspect to inspect is the difference obtained in the solution by increasing the size of the domain along the spanwise direction, which may improve the quality of the statistics because it permits to describe the streaks with more accuracy.
Therefore, three different domains will be simulated, with a dimension of 6, 8 and 10 non-dimensional units respectively, keeping the same value of non-dimensional spacing Δz^+.
We want to stress that the grid is uniform along z, so the number of points will increase linearly with the size.
The correct number of points is obtained by means of a dedicated program that permits to evaluate the values of Δx^+, Δy^+ and Δz^+, knowing the number of grid points and the sizes of the domain along each direction, given the distribution of the grid and the reference friction Reynolds number.
Moreover, it is possible to initialise each simulation starting from results (after a fixed number of iterations) related to only one of the grids tested.
Then, with a dedicated program developed by Ing. De Vanna, we can interpolate trends of the observed quantities to grids with different resolutions and sizes.
This permits to bypass the transitory flow behaviour and significantly reduce the solution times.
So, 50000 iterations are carried out starting from the domain with Δz = 6: then, such partial solution is interpolated on the other grids.
It is supposed to reach the convergence with 200000 iterations in total.
The three grids are summarised in detail below.

Grid dimension	**Number of points**	**Non-dimensional spacing**
x_{min} = 0	n_x = 512	Δx^+ = 31.64
x_{max} = 90		
y_{min} = 0	n_y = 128	Δy^+ = 0.7
y_{max} = 10		
z_{min} = -3	n_z = 52	Δz^+ = 20.77
z_{max} = +3		

Table 5.1: Data for a span of 6 non-dimensional units along z

Grid dimension	Number of points	Non-dimensional spacing
x_{min} = 0	n_x = 512	Δx^+ = 31.64
x_{max} = 90		
y_{min} = 0	n_y = 128	Δy^+ = 0.7
y_{max} = 10		
z_{min} = -4	n_z = 70	Δz^+ = 20.57
z_{max} = +4		

Table 5.2: Data for a span of 8 non-dimensional units along z

Grid dimension	Number of points	Non-dimensional spacing
x_{min} = 0	n_x = 512	Δx^+ = 31.64
x_{max} = 90		
y_{min} = 0	n_y = 128	Δy^+ = 0.7
y_{max} = 10		
z_{min} = -5	n_z = 88	Δz^+ = 20.45
z_{max} = +5		

Table 5.3: Data for a span of 10 non-dimensional units along z

5.3 Analyses of the grid resolution along streamwise direction

In order to inspect the effect of the grid resolution along x, three different grids are used, varying the number of points along x and keeping the same size of the domain in this direction.
Values of Δx^+ of 20, 31.64, 40 are imposed.
As in the previous case, the three simulations are initialised starting from the results of the first simulation after 50000 iterations, and it's supposed to reach the convergence after 200000 iterations in total.

Data of the grids are described in the space below.

Grid dimension	Number of points	Non-dimensional spacing
x_{min} = 0	n_x = 512	Δx^+ = 31.64
x_{max} = 90		
y_{min} = 0	n_y = 128	Δy^+ = 0.7
y_{max} = 10		
z_{min} = -3	n_z = 52	Δz^+ = 20.77
z_{max} = +3		

Table 5.4: Data for a spacing of 32 non-dimensional units along x

Grid dimension	Number of points	Non-dimensional spacing
x_{min} = 0	n_x = 404	Δx^+ = 40.10
x_{max} = 90		
y_{min} = 0	n_y = 128	Δy^+ = 0.7
y_{max} = 10		
z_{min} = -3	n_z = 52	Δz^+ = 20.77
z_{max} = +3		

Table 5.5: Data for a spacing of 40 non-dimensional units along x

Grid dimension	Number of points	Non-dimensional spacing
x_{min} = 0	n_x = 808	Δx^+ = 20.05
y_{max} = 90		
y_{min} = 0	n_y = 128	Δy^+ = 0.7
x_{max} = 10		
z_{min} = -3	n_z = 52	Δz^+ = 20.77
z_{max} = +3		

Table 5.6: Data for a spacing of 20 non-dimensional units along x

5.4 Analyses of the grid resolution along spanwise direction

As in the previous case, we want to inspect the effect of the grid resolution along the z-axis, so different grids are used, varying the number of points along the z-axis and maintaining the same size of the domain in this direction.
In this case-study, values of Δz^+ of 20, 15, 10 are imposed.
Initialisation is managed as said previously.

In the next tables the details of the grids are summarised.

Grid dimension	Number of points	Non-dimensional spacing
x_{min} = 0	n_x = 404	Δx^+ = 40.10
x_{max} = 90		
y_{min} = 0	n_y = 128	Δy^+ = 0.7
y_{max} = 10		
z_{min} = -3	n_z = 52	Δz^+ = 20.77
z_{max} = +3		

Table 5.7: Data for a spacing of 21 non-dimensional units along z

Grid dimension	Number of points	Non-dimensional spacing
x_{min} = 0	n_x = 404	Δx^+ = 40.10
x_{max} = 90		
y_{min} = 0	n_y = 128	Δy^+ = 0.7
y_{max} = 10		
z_{min} = -3	n_z = 72	Δz^+ = 15.0
z_{max} = +3		

Table 5.8: Data for a spacing of 15 non-dimensional units along z

Grid dimension	Number of points	Non-dimensional spacing
x_{min} = 0	n_x = 404	Δx^+ = 40.10
x_{max} = 90		
y_{min} = 0	n_y = 128	Δy^+ = 0.7
y_{max} = 10		
z_{min} = -3	n_z = 108	Δz^+ = 10.0
z_{max} = +3		

Table 5.9: Data for a spacing of 10 non-dimensional units along z

5.5 Analyses of grid resolution along wall-normal direction

We want to analyse the influence of grid resolution along the wall-normal direction.
Therefore, several grids with different nodes number along y are tested, by imposing Δy^+ = 20, 30 and 40.
Differently from the previous cases, it's not possible to carry out the simulations simply by changing the number of points because, as we said before, the wall-normal direction is characterised by strong variations of quantities that define the kinematic and thermal fields.
So, a high number of nodes is requested to capture these motions and, consequently, to solve the boundary layer.
An alternative approach consists in renouncing to solve the inner layer, that will be modelled, resolving only the outer one: such technique is called *wall-modelling* and is discussed in detail in the next chapter.
Hence, three simulations are carried out till the convergence, testing for each of these two different models for the inner layer.

In the next tables details of the grids are summarised.

Grid dimension	**Number of points**	**Non-dimensional spacing**
x_{min} = 0	n_x = 300	Δx^+ = 54.00
x_{max} = 90		
y_{min} = 0	n_y = 90	Δy^+ = 20.00
y_{max} = 10		
z_{min} = -3	n_z = 22	Δz^+ = 49.09
z_{max} = +3		

Table 5.10: Data for a spacing of 20 non-dimensional units along y

Grid dimension	**Number of points**	**Non-dimensional spacing**
x_{min} = 0	n_x = 300	Δx^+ = 54.00
x_{max} = 90		
y_{min} = 0	n_y = 60	Δy^+ = 30.00
y_{max} = 10		
z_{min} = -3	n_z = 22	Δz^+ = 49.09
z_{max} = +3		

Table 5.11: Data for a spacing of 30 non-dimensional units along y

Grid dimension	**Number of points**	**Non-dimensional spacing**
x_{min} = 0	n_x = 300	Δx^+ = 54.00
x_{max} = 90		
y_{min} = 0	n_y = 46	Δy^+ = 39.13
y_{max} = 10		
z_{min} = -3	n_z = 22	Δz^+ = 49.09
z_{max} = +3		

Table 5.12: Data for a spacing of 40 non-dimensional units along y

Chapter 6

Wall-modelled LES of boundary layer

6.1 Introduction to wall-modelling

The most important problem related to turbulent boundary layer is its multi-scale nature [18], from which the turbulent kinetic energy is carried by eddies of different characteristic sizes in layers near and far from the wall.
The idea of wall modelled LES is to respect the dynamic of the boundary layer structure by resolving only the energetic eddies in the outer layer (that are the largest and the most energetic ones), where they are almost Reynolds independent [14], modelling instead all eddies in the inner layer, where they are smaller.
Therefore, all the inner layer dynamics (streaks, quasi-streamwise vortices, peak production and dissipation, etc.) are removed from the resolution system and represented by a single value of the wall shear stress τ_w in the case of incompressible flow, in addition to the wall heat flow q_w in the case of compressible flow.
Such a strong simplification of the dynamics highly reduces the computational cost associated to the solution of the phenomenon, because the grid resolution requirements are no more linked to the small eddies of the inner layer, but to the larger eddies of the outer one.
It is worth noting that the outer layer turbulence in wall-modelled LES is produced and then dissipated in the outer layer itself, as it should be in high Reynolds wall turbulence [1], even if the peak of production region is the inner layer.
WMLES is meaningful only at sufficiently high Reynolds number, for which the boundary layer has a clear multi-scale character, with a separation of scales between the inner and the outer layers that justifies such an approach [18].
Indeed, a high-turbulent behaviour implies that most of computational resources are spent on the viscous and logarithmic layers.
So, LES will be almost as costly as DNS for boundary layers flows: this cost-scaling is the "near-wall problem" of LES.
Wall modelled LES methods can be subdivided into two different techniques, that is, Hybrid LES/RANS and Wall-stress modelling.
In hybrid LES/RANS methods, the LES region exists only above an "interface" y_{int}, while in the region below y_{int} the RANS approach is used.
In contrast, in the wall-stress modelling approach the LES is formally defined as extending all the way down to the wall, but it is solved on a grid that only resolves the outer layer motions. A wall model takes as input the istantaneous LES solution at a height $y = h_{wm}$ above the wall and estimates the instantaneous shear stress τ_w and the instantaneous wall heat flux q_w at the wall $y = 0$, that are then given back to the LES as boundary conditions.
Generally, the wall model is based on RANS concept of differing fidelities (e.g. with or without

[1] where the Reynolds stress have been found to be predominantly produced at the same wall distance as they are later dissipated [12]

equilibrium assumptions).
Errors in wall-modelling can be subdivided into two categories: errors in the wall-model itself and errors in the LES concerning the first few grid points next to the wall (that are usually chosen to get data from the LES solution).
This last kind of error derives from the fact that LES is necessarily underresolved in these points, so associated numerical and subgrid modelling errors can't be avoided [14].
The present work aims to realise a simple algebraic wall-stress model to solve a supersonic turbulent boundary layer with high values of Δy^+ and saving much computational resources.
Its peculiar feature is that it will be implemented by using finite differences instead of finite volumes[2].
So, wall shear stress and wall heat flow can't be imposed directly as in finite-volumes approach.
A differential wall-stress model, already realised for turbulent channels and then readapted for turbulent boundary layer, will be also tested in order to make a direct comparison with the previous one and with DNS results.

6.2 Algebraic Wall-Stress Model

The simplest wall-stress model to solve the near-wall problem is the algebraic one.
The aim is to model the turbulent eddies into the inner layer just to obtain shear stress and heat flux boundary conditions at the wall. In general, these values will be not physically realistic, but they will permit to obtain the correct dynamics in the outer layer without solving any differential equation for the entire modelled layer.
The proposed wall-model is based on the knowledge of the mean streamwise velocity profile, $\bar{u}^+$, of a incompressible wall flow within the log-layer ($y^+ > 30$). It can be described by the well-known *log law* by Von Karman, according to which:

$$\bar{u}^+ = \frac{1}{k} ln(y^+) + B \tag{6.2.1}$$

where

- $k \approx 0.41$ is the Von Karman constant
- $B \approx 5.2$ is another constant
- $\bar{u}^+ = \frac{\bar{u}}{u_\tau}$ is the definition of the non-dimensional streamwise mean velocity
- u_τ is the instantaneous local friction velocity
- $y^+ = \frac{y}{\delta_\nu} = \frac{\rho_w u_\tau y}{\mu_w}$ is the non-dimensional wall distance, with ρ_w and μ_w the density and the molecular dynamic viscosity at the wall, respectively.

From equation (6.2.1) we can deduct that, once fixed the y-coordinate [3], we have:

$$\bar{u}^+ - \frac{1}{k} ln\Big(\frac{\rho_w u_\tau y}{\mu_w}\Big) - B = 0 = f(u_\tau) \tag{6.2.2}$$

Hence, it's necessary to solve an implicit function's zero problem to get the u_τ. In this work the Newton-Raphson approach has been used.
Thus, the wall shear stress can be calculated by definition:

$$\tau_w = \rho_w u_\tau^2 \tag{6.2.3}$$

[2] technique that is usually used in this framework
[3] suitably coincident with the LES-node y-coordinate from which data is taken as input for the wall model

Such a condition should be already used to solve a problem of incompressible turbulent boundary layer.
However, for a compressible one also the wall heat flux must be imposed as boundary condition.
It's convenient to follow a very similar approach, by finding the temperature profile in the wall model from the velocity profile.
Once the temperature profile is known, it's possible to evaluate the wall heat flux q_w by imposing:

$$q_w = \Big[\lambda\Big(\frac{\partial T}{\partial y}\Big)_{wm}\Big]_w = \Big[c_p\frac{\mu}{Pr}\Big(\frac{\partial T}{\partial y}\Big)_{wm}\Big]_w \tag{6.2.4}$$

where the subscript 'wm' denotes quantities modelled in the wall model, 'w' indicates quantities evaluated at the wall, λ is the thermal conductivity.

Nevertheless, this definition is not appropriate for the boundary conditions application if the wall is adiabatic. So, another alternative is adopted, as proposed in [43].
According to this

$$q_w = \Big[u_{\parallel}\tau_w + c_p\frac{\mu_{t,wm}}{Pr_{t,wm}}\frac{\partial T}{\partial y}\Big]_{y=h_{wm}} \tag{6.2.5}$$

where $u_{\parallel}$ is the total wall-parallel velocity including both streamwise and spanwise components, $\mu_{t,wm}$ and $Pr_{t,wm} = 0.9$ are the wall-modelled eddy viscosity and turbulent Prandtl number.
This expression derives from the integral of the one-dimensional total-energy conservation equation along the wall-normal direction, evaluated at the matching location h_{wm}. It considers the sum of the aerodynamic heating, the molecular heat conduction and the turbulent heat transport[4].
It's worth noting that, according to (6.2.5), in adiabatic conditions (i.e., $q_w = 0$) the slope of the temperature at the edge of the wall-modelled layer is not necessarily zero in high-speed conditions.
The temperature profile in the wall layer can be evaluated by using the well-known turbulent Crocco-Busemann relation [40](see Appendix C for details):

$$\bar{T} \approx T_w + (T_{aw} - T_w)\frac{\bar{u}}{U_\infty} - r\frac{\bar{u}^2}{2c_p} \tag{6.2.6}$$

valid for $Pr \approx Pr_t \approx 1$ (approximatively true for air) and negligible pressure gradient, where $\bar{u}$ is the mean streamwise velocity in compressible turbulent conditions, T_{aw} is the adiabatic wall temperature, r is the recovery factor.
Nevertheles, such definition is implicit, because it's necessary to know the mean velocity profile (that is, in turn, unknown) to model the temperature profile.
Therefore, a convergence iterative process is used to get the correct velocity profile, and so the temperature one.
The incompressible mean velocity profile is gradually revised by imposing a Van Driest style correction, according to which:

$$\bar{u}_j = \bar{u}_{j-1} + \frac{1}{2}\Big(\sqrt{\frac{\rho_w}{\rho_j}} + \sqrt{\frac{\rho_w}{\rho_{j-1}}}\Big)(\bar{u}_{inc,j} - \bar{u}_{inc,j-1}) \tag{6.2.7}$$

where the subscripts 'j' and 'j-1' refers to the velocity value at nodes 'j' ad 'j-1' of the wall-model grid along the wall-normal direction, respectively.
The density profile in (6.2.7) is modelled by imposing the state law, according to which:

$$\rho = p/RT = f(T) \tag{6.2.8}$$

So, this is a function of the temperature only, being the pressure constant along the wall-normal direction within the inner layer.

[4] where the molecular heat conduction has been neglected because $\mu/\mu_{t,wm} = O(\delta_\nu/h_{wm}) \ll 1$

The wall model region is discretized with a denser grid (30 nodes) along the wall normal direction compared to the LES one, and it spans from the wall $y = 0$ to a matching location $y = h_{wm}$ where the wall-model solution matches with the LES solution on the coarser grid.

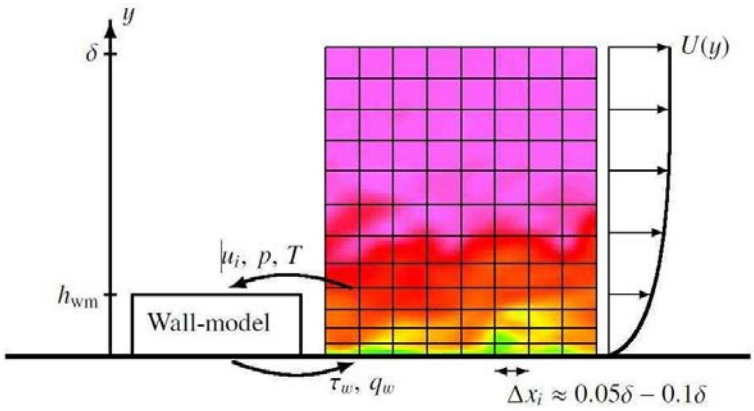

Figure 6.1: Representation of the wall-stress modelling approach

Following Kawai and Larsson [14], the matching location is set to $h_{wm} = 2.5\Delta y$, where Δy is the WMLES grid spacing in wall-normal direction.
This matching height corresponds to the third LES grid point from the wall, and of course it is chosen to fall within the log-layer.

6.3 Differential Wall Stress Model

The differential model used in this works, and proposed by Kawai and Larsson [18] [43], is an ODE-based wall-stress model.
We consider the case of an equilibrium model for compressible flow, for which the one-dimensional momentum and total energy equations are:

$$\frac{d}{dy}\Big[(\mu + \mu_{t,wm})\frac{du_{\parallel}}{dy}\Big] = 0 \tag{6.3.1}$$

$$\frac{d}{dy}\Big[c_p\Big(\frac{\mu}{Pr} + \frac{\mu_{t,wm}}{Pr_{t,wm}}\Big)\frac{dT}{dy}\Big] = -\frac{d}{dy}\Big[(\mu + \mu_{t,wm})u_{\parallel}\frac{du_{\parallel}}{dy}\Big] \tag{6.3.2}$$

and the wall-model eddy-viscosity is taken as:

$$\mu_{t,wm} = k\rho\sqrt{\frac{\tau_w}{\rho}}y\Big[1 - e^{-\frac{y^+}{A^+}}\Big]^2 \tag{6.3.3}$$

with $k = 0.41$, $Pr_{t,wm} = 0.9$ and $A^+ = 17$.
Density and temperature are related through the equation of state:

$$p = \rho RT \tag{6.3.4}$$

where the static pressure, p, is assumed constant across the wall-modelled region.
These equations must be solved over the region $0 \leq y \leq h_{wm}$.
At the top boundary, $u_{\parallel}$ is set to be equal to the magnitude of the wall-parallel velocity in the LES, while T is taken directly from the LES.
At the wall, the no-slip condition is applied, together with the condition of adiabatic wall.

As in the previous model, once the system of the two coupled ODEs is solved, the wall shear stress, τ_w, and the wall heat flux, q_w, can be directly computed and fed back to LES as boundary conditions at the wall.
Such quantities are evaluated as in the previous model.

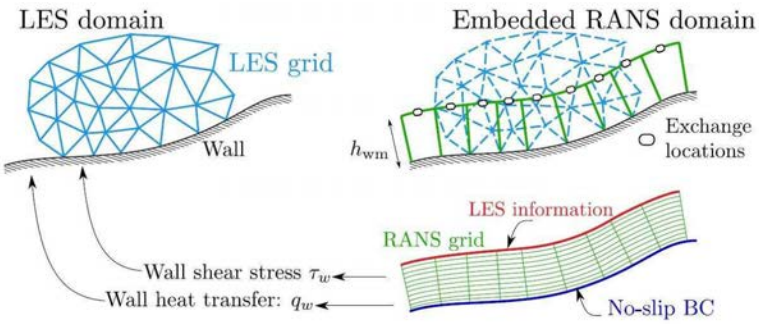

Figure 6.2: Representation of the differential wall-stress modelling approach

It's worth noticing that equation (6.3.2) is derived from the conservation of total energy. Therefore, this equation contains the effect of viscous heating.

Chapter 7

Boundary Conditions

7.1 Introduction

In this chapter boundary conditions are described.
In the Favre-filtered Navier-Stokes system of equations an initial condition for the conservative variables and a set of conditions at the limits must be specified.
As we said in previous chapters, LES treats with three-dimensional fluid domains, so 6 different interfaces with the outer environment must be defined.

Referring to figure 7.1, the interfaces can be subdivided in:

1. inlet boundary
2. upper boundary
3. bottom boundary
4. outlet boundary
5. right boundary
6. left boundary

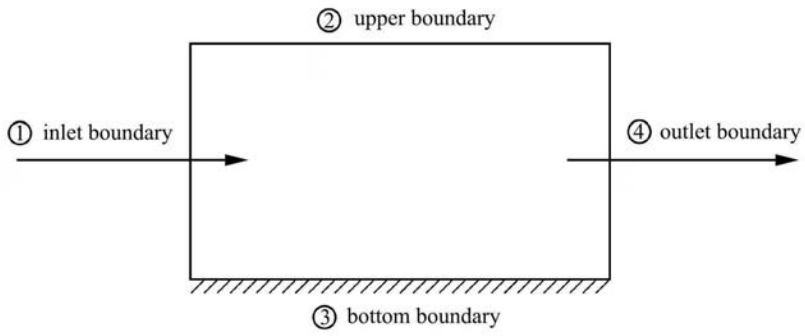

Figure 7.1: Boundaries of the domain. 5th and 6th interfaces are in the third dimension and are right and left boundaries, respectively

For each of these, one or more conditions must be defined to generate a computational closed domain. Since the flow is compressible, first LODI approximation is introduced. Then each condition is described.

7.2 Local One Dimension Approximation

The main problem in the definition of the boundary conditions for compressible flows is the strongly hyperbolic character of the Navier-Stokes equations [7].
In general, hyperbolic equations don't require boundary conditions, but only initial conditions: the latter will propagate autonomously both in space and time without any other specifications.
Moreover, because of the compressibility, the acoustic effects are inherent to the system's dynamics: therefore, the flow variables tend to reflect at the boundary locations, producing unphysical waves and oscillations [6].
Following the idea of Pirozzoli and Colonius [30], we want to present the one-dimensional inviscid approximation.
So, the associated purely hyperbolic problem (Euler's equations) is considered.
Let us highlight that the necessity of calculating the derivatives at nodes next to the boundary [1] crashes against the mathematical nature of the governing equations of the phenomenon.
To overcome such a problem, it's convenient to express the Euler's equations with their characteristic formulation.

These equations can be expressed using a matrix formulation as:

$$\frac{\partial \mathbf{U}}{\partial t} = -\frac{\partial \mathbf{F}_j(\mathbf{U})}{\partial x_j} \tag{7.2.1}$$

With an almost-linear formulation, equations (7.2.1) become:

$$\frac{\partial \mathbf{U}}{\partial t} = -A_j(\mathbf{U})\frac{\partial \mathbf{U}}{\partial x_j} \tag{7.2.2}$$

It's possible to prove that the Jacobian matrices $A_j = \partial \mathbf{F}_j(\mathbf{U})/\partial \mathbf{U}$ are non-singular.

Therefore, making explicit the eigenvalues matrices, equations (7.2.2) can be written as:

$$\frac{\partial \mathbf{U}}{\partial t} = -R^j \Delta^j L^j \frac{\partial \mathbf{U}}{\partial x_j} \tag{7.2.3}$$

where R^j and L^j are the j-th right and left eigenvectors matrices, while Δ^j is the diagonal eigenvalues matrix associated to the j-th flux, respectively.
This formulation is also known as *Euler's equations characteristic formulation*.

We can prove that the j-th eigenvalues matrix can be expressed as:

$$\Delta^j = \begin{pmatrix} u_j - c & 0 & 0 & 0 & 0 \\ 0 & u_j & 0 & 0 & 0 \\ 0 & 0 & u_j & 0 & 0 \\ 0 & 0 & 0 & u_j & 0 \\ 0 & 0 & 0 & 0 & u_j + c \end{pmatrix} \tag{7.2.4}$$

It's worth noting that eigenvalues represent the velocities whith whom information moves in the domain. Instead, eigenvectors represent locally the directions of the characteristic curves along which information moves.
Defining:

$$\mathcal{L}_j = \Delta^j L^j \frac{\partial \mathbf{U}}{\partial x_j} \tag{7.2.5}$$

eq. (7.2.3) can be express as:

[1] using the ghost nodes in finite differences

$$\frac{\partial \mathbf{U}}{\partial t} = -R^j \mathcal{L}_j \tag{7.2.6}$$

These vectors $\mathcal{L}_j$ contain the characteristic waves (i.e., primitive-variables' derivatives combinations) associated to the flux component $\mathbf{F}_j(\mathbf{U})$.

For the x-component [7]:

$$\mathcal{L}_x = \begin{bmatrix} \lambda_1\left(\frac{\partial p}{\partial x} - \rho c \frac{\partial u}{\partial x}\right) \\ \lambda_2\left(c^2 \frac{\partial \rho}{\partial x} - \frac{\partial p}{\partial x}\right) \\ \lambda_3 \frac{\partial v}{\partial x} \\ \lambda_4 \frac{\partial w}{\partial x} \\ \lambda_1\left(\frac{\partial p}{\partial x} + \rho c \frac{\partial u}{\partial x}\right) \end{bmatrix} \tag{7.2.7}$$

It's important to remember that the ideal boundary condition mustn't perturb the physics of the phenomenon. So, it's an information that must be imposed as far as possible from the interesting regions in the domain.
Thus, it's reasonable to assume that, next to the boundary, the transverse terms are not very important, so eq. (7.2.6) can be expressed as:

$$\frac{\partial \mathbf{U}_b}{\partial t} = -(R^x \mathcal{L}_x)_b \tag{7.2.8}$$

Such formulation is called **Local One-Dimensional Inviscid Approximation** (LODI) and permits to define the boundary conditions of the problem.

By expanding (7.2.7), we have:

$$\frac{\partial \rho}{\partial t} = -d_1 \tag{7.2.9}$$

$$\frac{\partial(\rho u_1)}{\partial t} = -u_1 d_1 - \rho d_3 \tag{7.2.10}$$

$$\frac{\partial(\rho u_2)}{\partial t} = -u_2 d_2 - \rho d_4 \tag{7.2.11}$$

$$\frac{\partial(\rho u_3)}{\partial t} = -u_3 d_3 - \rho d_3 \tag{7.2.12}$$

$$\frac{\partial(\rho E)}{\partial t} = -\frac{1}{2} u_i u_i d_1 - \frac{d_1}{\gamma - 1} - u_1 d_1 - \rho u_1 d_3 - \rho u_2 d_4 - \rho u_3 d_5 \tag{7.2.13}$$

where

$$\mathbf{d} = \begin{bmatrix} \frac{1}{c^2}(\mathcal{L}_2 + \frac{1}{2}(\mathcal{L}_5 + \mathcal{L}_1)) \\ \frac{1}{2}(\mathcal{L}_5 + \mathcal{L}_1) \\ \frac{1}{2\rho c}(\mathcal{L}_5 - \mathcal{L}_1) \\ \mathcal{L}_3 \\ \mathcal{L}_4 \end{bmatrix} \tag{7.2.14}$$

Hence, this approach is helpful to overcome problems related to Euler's equations boundary conditions in finite-differences technique.

7.3 Supersonic inflow

In the present work the flow is supersonic at the inlet and it is moving into the domain. So, the characteristic velocities (i.e. eigenvalues of the Jacobian matrix) are:

$$\lambda_1 = u - c > 0 \tag{7.3.1}$$
$$\lambda_2 = u > 0 \tag{7.3.2}$$
$$\lambda_3 = u > 0 \tag{7.3.3}$$
$$\lambda_4 = u > 0 \tag{7.3.4}$$
$$\lambda_5 = u + c > 0 \tag{7.3.5}$$

Since all velocities are positive, all information needed to define the boundary condition should come from the outer of the domain. So, five independents quantities must be fixed. In this case they are:

$$\rho_b = \rho(y, z, t) = \bar{\rho} + \rho' \tag{7.3.6}$$
$$(u_i)_b = u_i(y, z, t) = \tilde{u}_i + u_i' \tag{7.3.7}$$
$$T_b = T(y, z, t) = \tilde{T} + T' \tag{7.3.8}$$
$$\tag{7.3.9}$$

where for each quantity (density, velocity and temperature respectively) the resolved and the subgrid-scale terms are made explicit.
The different profiles are obtained using the digital filter approach by Klein (2003) [15][41].

7.4 Supersonic Outflow

Since there are not any shock waves along the flat plate, the outlet condition is about a supersonic outflow.
In this case, the characteristic velocities are:

$$\lambda_1 = u - c > 0 \tag{7.4.1}$$
$$\lambda_2 = u > 0 \tag{7.4.2}$$
$$\lambda_3 = u > 0 \tag{7.4.3}$$
$$\lambda_4 = u > 0 \tag{7.4.4}$$
$$\lambda_5 = u + c > 0 \tag{7.4.5}$$

Since each of these velocities is positive, all information to assign to the boundary should come from the inner of the domain.
This means that the discrete formulation must recover information from the inner nodes, in order to define the quantities on the ghost nodes.
Thanks to LODI formulation, the following equations:

$$\frac{\partial \mathbf{U}_b}{\partial t} = -(R^j \mathcal{L}_x)_b \tag{7.4.6}$$

can be integrated at the boundary.
Hence, upwind finite differences can be used to discretize the $\mathcal{L}_x$ waves.
In other words, the boundary conditions adapt to what happens into the domain.
This condition is imposed both in outlet and upper boundary, using the so called **Navier-Stokes Characteristic Boundary Conditions** (NSCBC), based on LODI Approximations.

7.5 Adiabatic wall

The simulation assumes that the plate is adiabatic and with no-slip.
Hence, velocity is set to zero at the wall and the *soft adiabatic condition* is imposed.
Under the following hypothesis:

- stationary flow in pressure
- out-of-boundary-layer analysis
- adiabatic system
- negligible mass forces

it follows that the total enthalpy h^0 is constant, with:

$$h^0 = c_P T^0 \tag{7.5.1}$$

So, also the total temperature T^0 is constant.
It's worth noticing that the total temperature is the maximum one of all the system, because it is the stagnation temperature.
In the case of adiabatic wall, the total temperature is the temperature at which the wall itself is, because at the wall the conditions of adherence and impermeability are imposed.
We can prove that in these conditions:

$$\frac{T^0}{T} = 1 + \frac{\gamma - 1}{2} M^2 \tag{7.5.2}$$

where T and M are the static temperature and the Mach number, respectively, at the point of the domain considered.

Anyway, the total temperature is reached at the wall, so into the boundary layer, where the viscous stress are very significant.
Thus, the previous hypothesis are not valid.
Eq. (7.5.2) can be modified by introducing the *recovery factor, r*, to consider also the viscous contribution, giving:

$$\frac{T^0}{T} = 1 + r\frac{\gamma - 1}{2} M^2 \tag{7.5.3}$$

where r is imposed from the thermodynamic.
The recovery factor can be defined as:

$$r = \frac{T_{aw} - T_\infty}{T_{0\infty} - T_\infty} \tag{7.5.4}$$

where T_{aw} is the adiabatic wall temperature.
Equation (7.5.4) shows that r represents the ratio between the increment of temperature due to the friction and the one due to an adiabatic compression.
Hence, this factor takes into account the reduction of T_{aw} with respect to $T_{0\infty}$ due to the viscous effects into the boundary layer (see figure (7.2)).

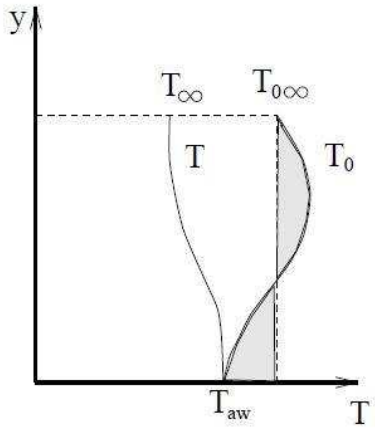

Figure 7.2: Trend of the total temperature into the boundary layer due to the viscous effects [1]. Please note that the two hatched areas must be equivalent.

In a laminar flow, if $Pr = 1$ you have that $r = 1$.
However, if $Pr \neq 1$, the recovery factor can be estimated as [1]:

$$r = Pr^{\frac{1}{2}} \tag{7.5.5}$$

for a wide range of temperatures, where Pr is the Prandtl number.

If the flow is turbulent, you have:

$$r = Pr^{\frac{1}{3}} \tag{7.5.6}$$

Hence, *recovery temperature* is the temperature at which the wall is in adiabatic condition, and it can be estimated with eq. (7.5.3).
In summary, by imposing the recovery temperature as wall temperature is equal to get a null-value gradient of temperature at the wall, obtaining the adiabatic condition.
It's worth noting that this is not an absolute condition, because eq. (7.5.6) is not obtained analytically but it is an experimental result. So, the wall temperature gradient will be on average zero, but it will swing around the null value.
As in the previous case, this condition is imposed by implementing the NSCBC.

7.5.1 Adiabatic wall for wall-stress model

When a wall-stress model is used to get the correct dynamics in the outer layer, values of the wall shear stress, τ_w, and wall heat flux, q_w, must be imposed at the wall.
With a finite-differences approach, the more convenient way is to define an effective molecular dynamic viscosity μ_{eff} and an effective thermal conductivity λ_{eff} as below:

$$\mu_{eff} = \mu_w \frac{\left(\partial U/\partial y\right)_{WM}}{\left(\partial \tilde{U}/\partial y\right)_{LES}} \tag{7.5.7}$$

$$\lambda_{eff} = \lambda_w \frac{\left(\partial T/\partial y\right)_{WM}}{\left(\partial \tilde{T}/\partial y\right)_{LES}} \tag{7.5.8}$$

where all derivates are evaluated at the wall.

So, physically these quantities are those ones that permit to obtain the correct τ_w and q_w at the wall starting from data taken from LES nodes to evaluate the derivatives.
In particular,

$$\tau_w = \Big[\mu\Big(\frac{\partial U}{\partial y}\Big)_{WM}\Big]_{wall} = \Big[\mu_{eff}\Big(\frac{\partial \tilde{U}}{\partial y}\Big)_{LES}\Big]_{wall} \tag{7.5.9}$$

$$q_w = \Big[\lambda\Big(\frac{\partial T}{\partial y}\Big)_{WM}\Big]_{wall} = \Big[\lambda_{eff}\Big(\frac{\partial \tilde{T}}{\partial y}\Big)_{LES}\Big]_{wall} \tag{7.5.10}$$

It's worth noticing that, if the real values of μ and λ are used to evaluate wall shear stress and wall heat flux (using data from the LES nodes for the derivatives), wrong values will be found, because the wall-normal grid spacing is not dense enough to capture the correct values of the flow quantities next to the wall.
Therefore, appropriate conditions of μ and λ at the ghost nodes are imposed so that, at the wall coordinate, the averaged values between grid nodes and their respective ghost nodes are those ones of μ_{eff} and k_{eff}.

7.6 Left and right boundary

The aim is to impose any conditions that permit to realise a simulation as if the plate extends indefinitely along the spanwise direction.
An elegant way is to impose a periodic condition, both at the left and right side of the domain. So, that which enters from one side leaves from the other.

Chapter 8

Analyses of the results

In this chapter, results of the different studies are proposed and discussed.
In particular, each analysis is compared to the correct statistics, given by Pirozzoli [29] and obtained through a DNS simulation.
All values that appear in the next figure are in non-dimensional formulation and refer to two different stations along the x-axis, where the friction Reynolds number, Re_τ, is 200 and 252.
In particular, within each plot the x coordinate is made non-dimensional with reference to the thickness of the boundary layer, δ_{99}.
Firstly, we want to observe the mean streamwise velocity profile and the Reynolds stress to varying of the y^+ coordinate on a logarithmic scale.
Moreover, for the wall-resolved simulations also trends of friction factor and friction Reynolds number, Re_τ, are proposed, to varying of the non-dimensional x coordinate.

8.1 Wall Resolved Boundary Layer Analyses

8.1.1 Comparison of results about analyses of the domain size along the z-axis

Non-dimensional mean velocity profiles are shown in figures (8.1) and (8.2), with reference to the stations in which Re_τ of 200 and 252, respectively.

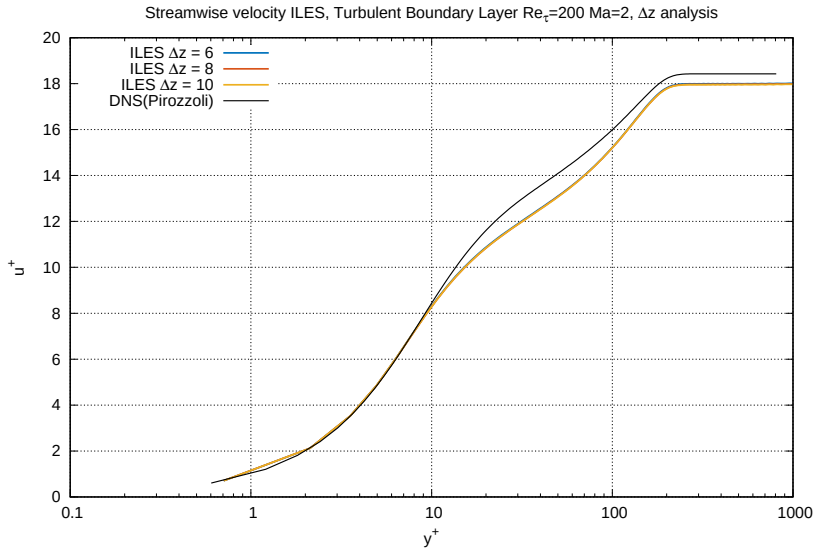

Figure 8.1: Mean velocity profiles with different domain spans related to Re_τ = 200

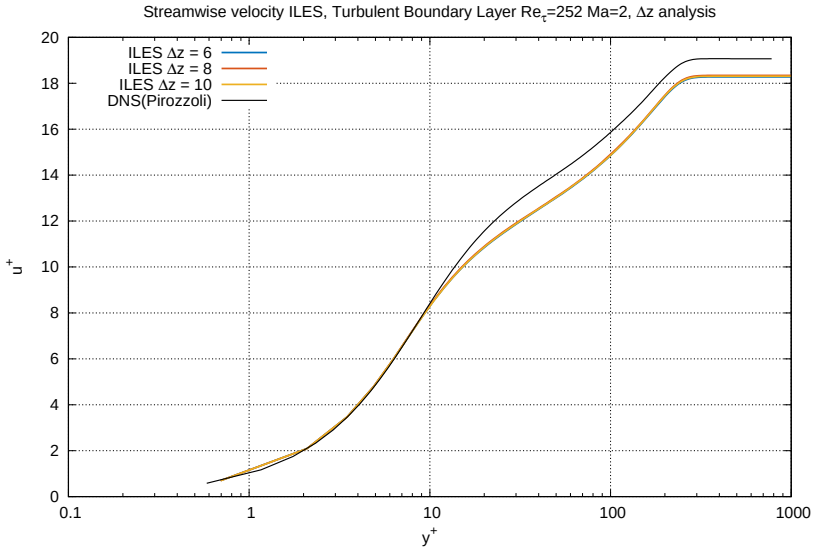

Figure 8.2: Mean velocity profiles with different domain spans related to Re_τ = 252

Trends appear almost the same to varying of the domain size along z. So, mean velocities seem quite insensitive to this parameter.
It's interesting to note that LES profiles differ from DNS ones by about 5 %.
Anyhow, results tend to underestimate the velocity far from the wall, especially for $Re_\tau = 252$.

Figures (8.3) and (8.4) are related to the Reynolds stress components, with reference to the previous stations.

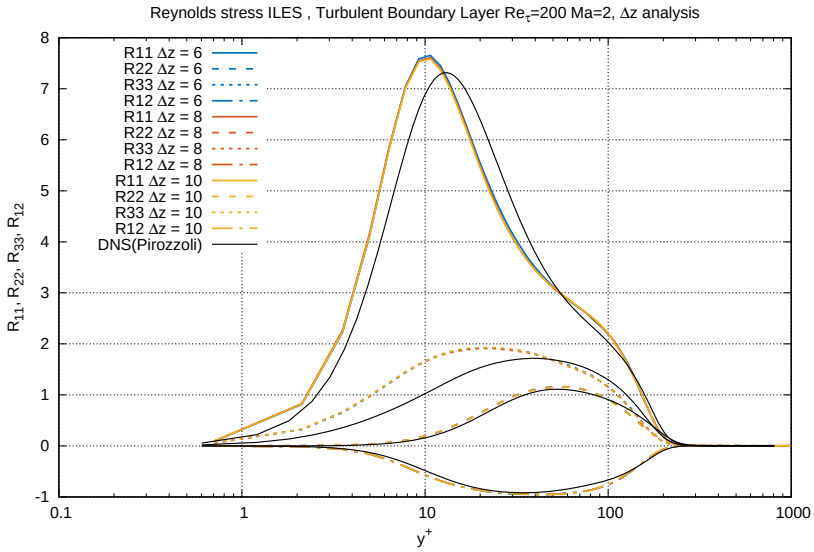

Figure 8.3: Reynolds stress with different domain spans related to Re_τ = 200

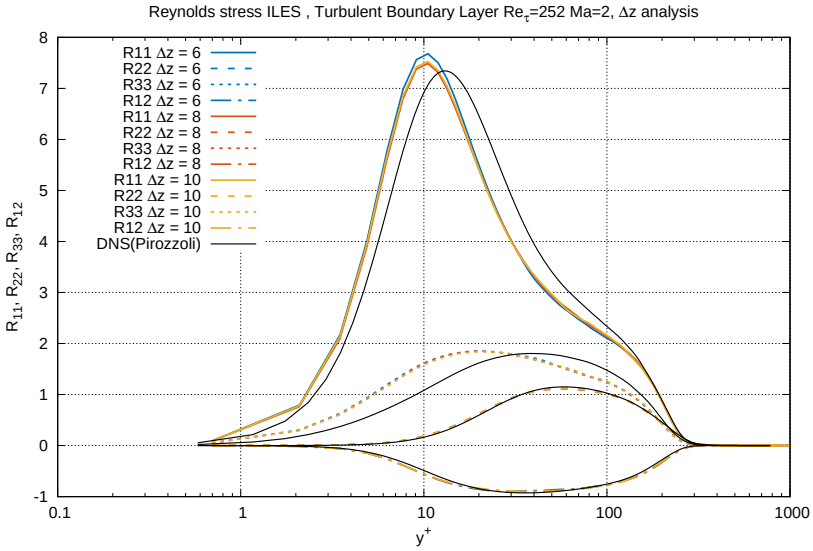

Figure 8.4: Reynolds stress with different domain spans related to Re_τ = 252

Trends show that also Reynolds stress are almost insensitive to the span along z.
In particular, only the first normal component shows a little variation as the domain span increases.
It's worth noting that all components of the Reynolds stress tensor have very similar trends compared to the DNS ones, except for the $< u'^2 >$ and $< w'^2 >$, which deviate more than the others.

Friction factor and Re_τ are reported in the next figures, in function of the non-dimensional x coordinate along the flat plate.

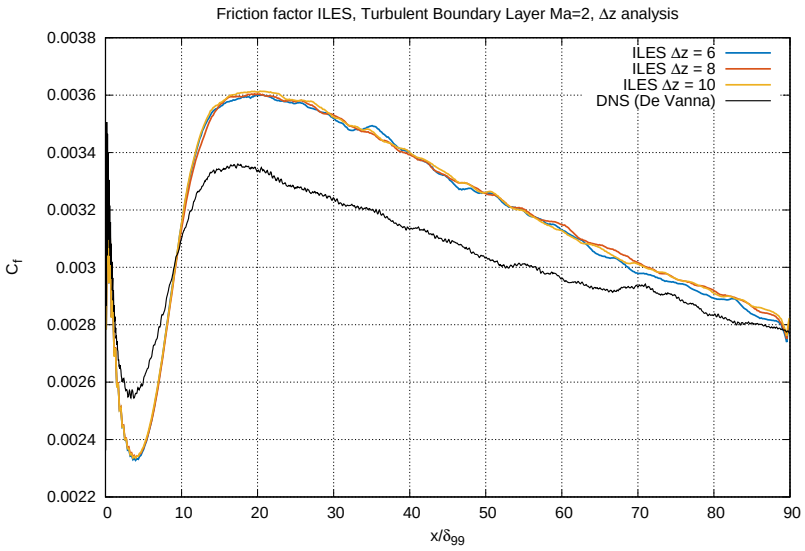

Figure 8.5: Friction factor with different domain spans along z

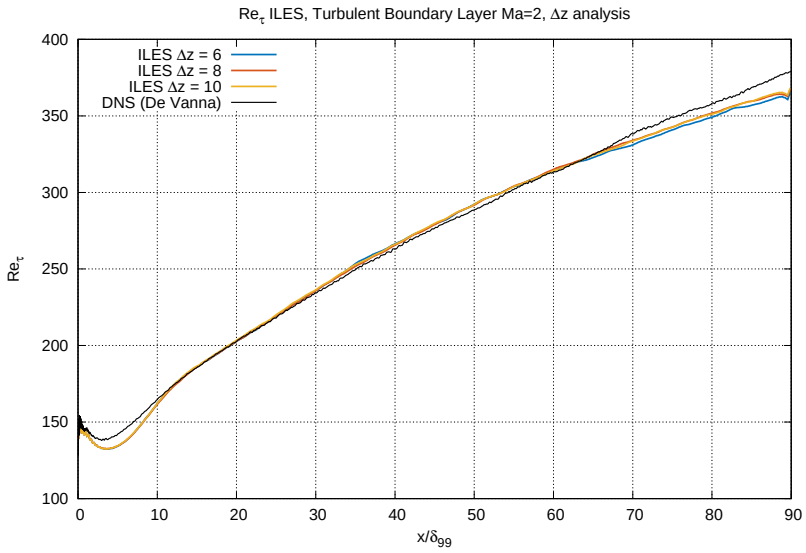

Figure 8.6: Re_τ with different domain spans along z

Starting from these figures, both friction factor and Re_τ are quite insensitive to the span along z for the chosen values of domain size.
It's worth noticing that both these parameters are wrongly predicted for small non-dimensional x coordinates: indeed, because of the inflow condition imposed, a small range at the leading edge is needed to get the correct turbulence of the flow.

In total, these analyses have proved that the accuracy of the solution seems not to be affected by spans along z that have been tested.
So, there's no advantage in enlarging the domain size in this direction more than the first case-study.

8.1.2 Comparison of results about analyses of the grid resolution along the x-axis

Non-dimensional mean velocity profiles are shown in figures (8.7) and (8.8), with reference to the stations in which Re_τ of 200 and 252 respectively.

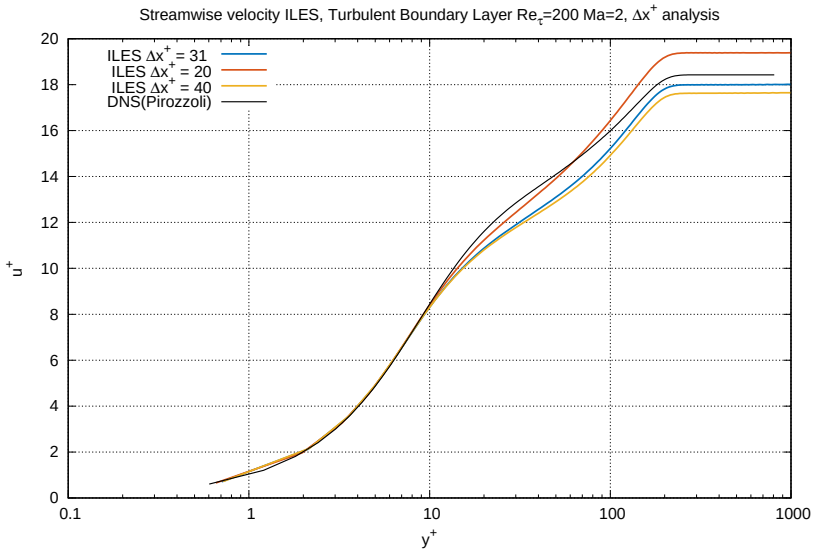

Figure 8.7: Mean velocity profiles with different grid resolutions related to Re_τ = 200

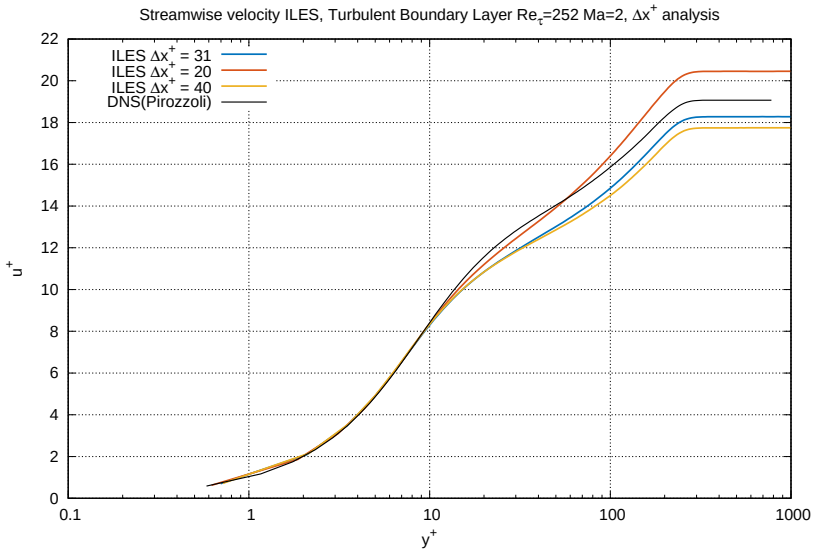

Figure 8.8: Mean velocity profiles with different grid resolutions related to Re_τ = 252

In general, an increase of the accuracy of the mean velocity profile is reached as the x-resolution increases.
However, it's interesting to notice that such advantage is obtained only near the wall ($y^+ \lesssim 100$).
A loss of accuracy can be observed farther from the wall in the case with Δx^+ = 20 compared to the case of Δx^+ = 31.64.
This phenomenon could be linked to non-linear effects related to the calculation.

In the space below, graphics related to the Reynolds stress components are proposed (figure (8.9) and

figure (8.10)).

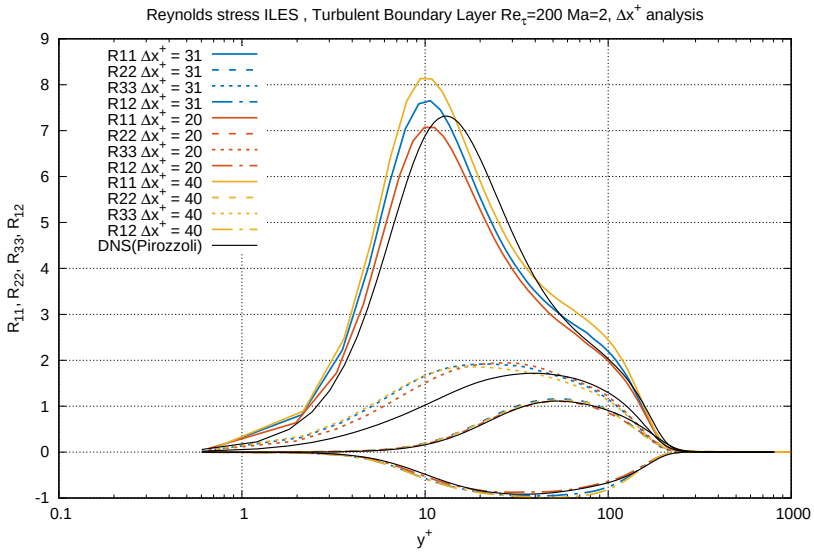

Figure 8.9: Reynolds stress with different grid resolutions related to Re_τ = 200

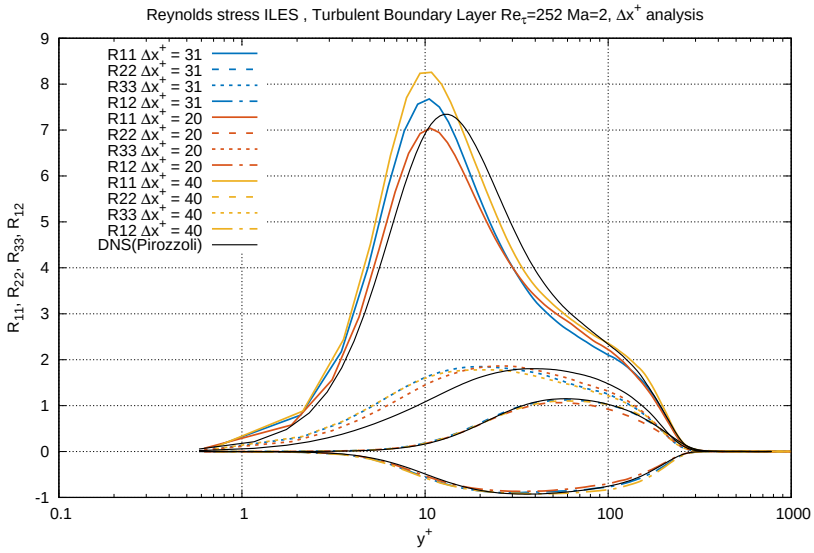

Figure 8.10: Reynolds stress with different grid resolutions related to Re_τ = 252

It is stressed an overall improvement of the solution accuracy as the resolution of the grid increases, with convergence towards values from DNS.
In particular, this effect is considerable with reference to the component $<u'^2>$.
Thus, it seems that both the mean velocity profiles and the Reynolds stress ones are much more sensitive to variations in grid resolution along the x-axis, compared to the previous analyses.

The trends of the friction factor and Re_τ are reported in figure (8.11) and (8.12), in function of the non-dimensional x-coordinate along the flat plate.

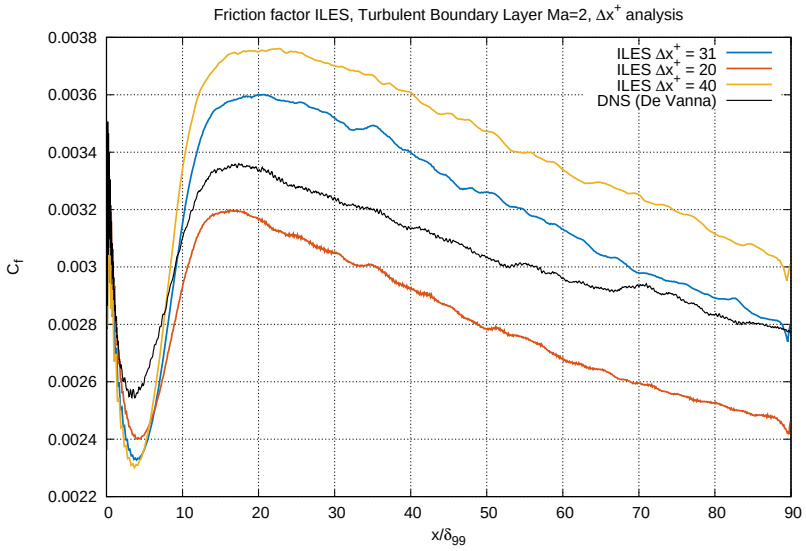

Figure 8.11: Friction factor with different grid resolutions along x

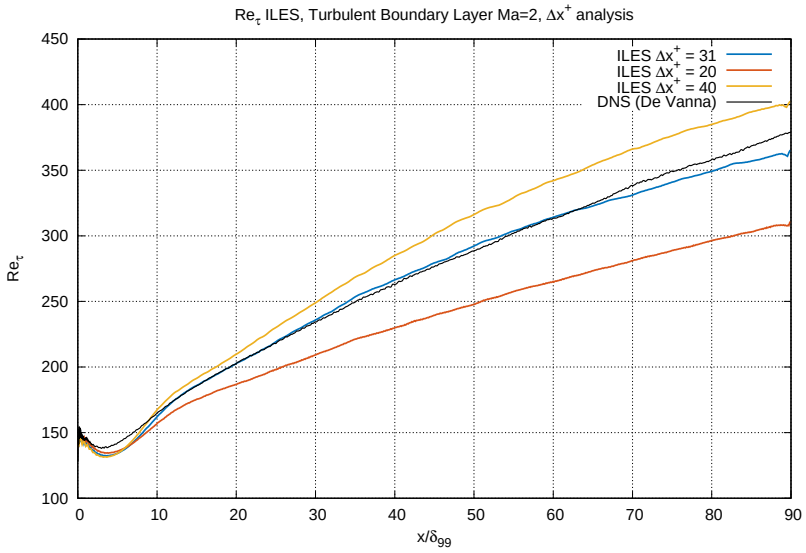

Figure 8.12: Re_τ with different grid resolutions along x

We can notice the rise of accuracy as the resolution increases, but again the most resolved case is still a bit distorted compared to DNS reference data.

8.1.3 Comparison of results about analyses of the grid resolution along the z-axis

Non-dimensional mean velocity profiles are shown in figures (8.13) and (8.14), with reference to the stations relative to Re_τ of 200 and 252 respectively.

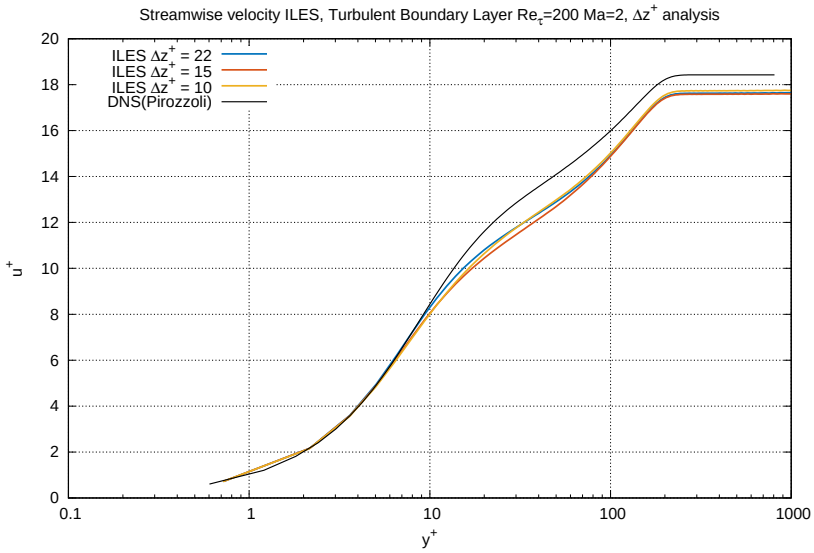

Figure 8.13: Mean velocity profiles with different grid resolutions related to Re_τ = 200

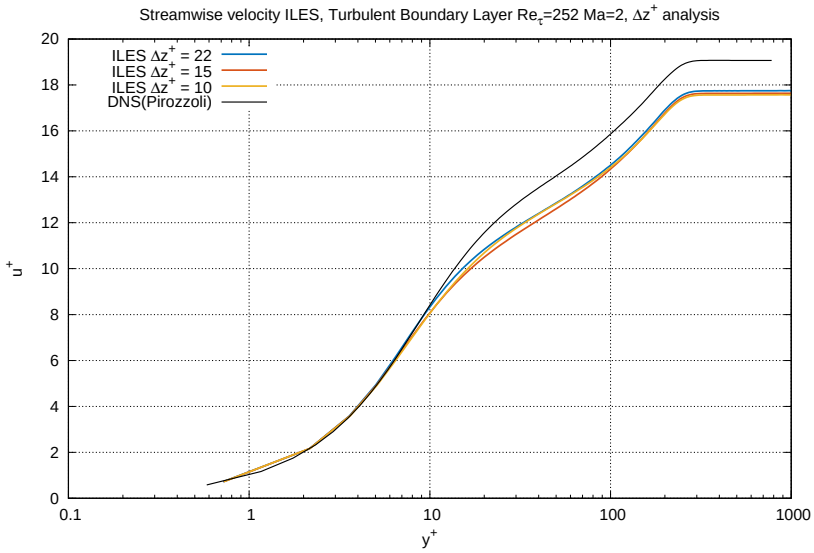

Figure 8.14: Mean velocity profiles with different grid resolutions related to Re_τ = 252

Differently from the analysis of grid resolution along the x-axis, the mean velocity profile seems to be insensitive to the resolution of the grid along the z-axis. Hence, the three trends collapse in only one profile. This can be observed in both the stations analysed.
However, it doesn't apply to the Reynolds stress, since figure (8.15) and figure (8.16) show that their profiles are strongly grid-resolution dependent.
Since a shorter range of Δz^+ has been tested compared to the Δx^+ analyses, Reynolds stress appear more sensitive to the Δz^+ value.
Thus, it becomes the most important parameter in this framework.

This is reasonable, since it influences the dynamics of the streaks that are described.

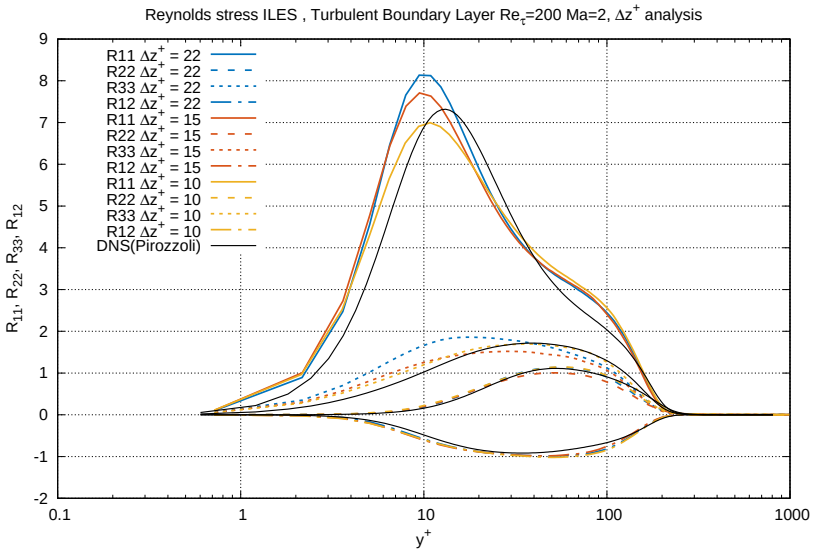

Figure 8.15: Reynolds stress with different grid resolutions related to Re_τ = 200

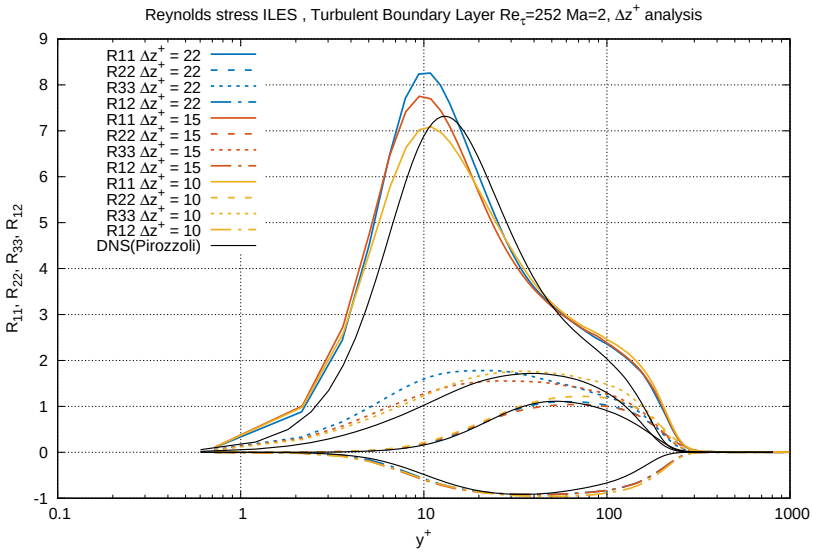

Figure 8.16: Reynolds stress with different grid resolutions related to Re_τ = 252

The trends of the friction factor and Re_τ are reported in the next figures, in function of the non-dimensional x-coordinate along the flat plate.

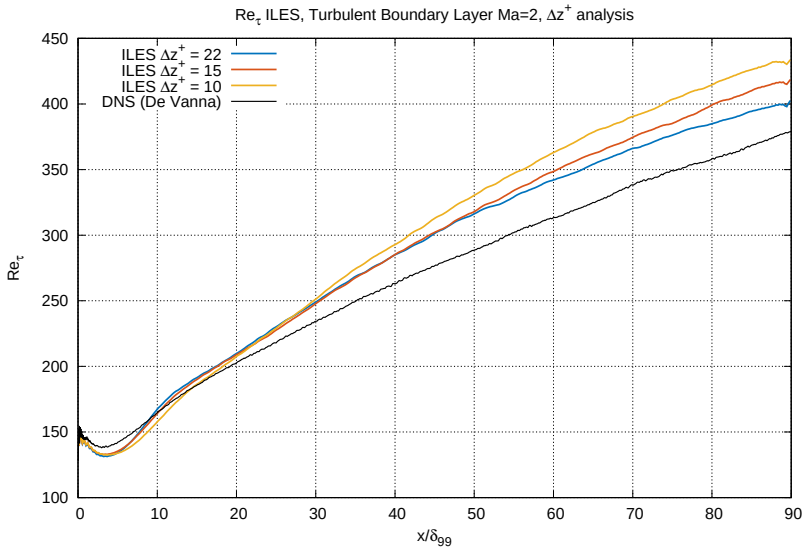

Figure 8.17: Re_τ with different grid resolutions along z

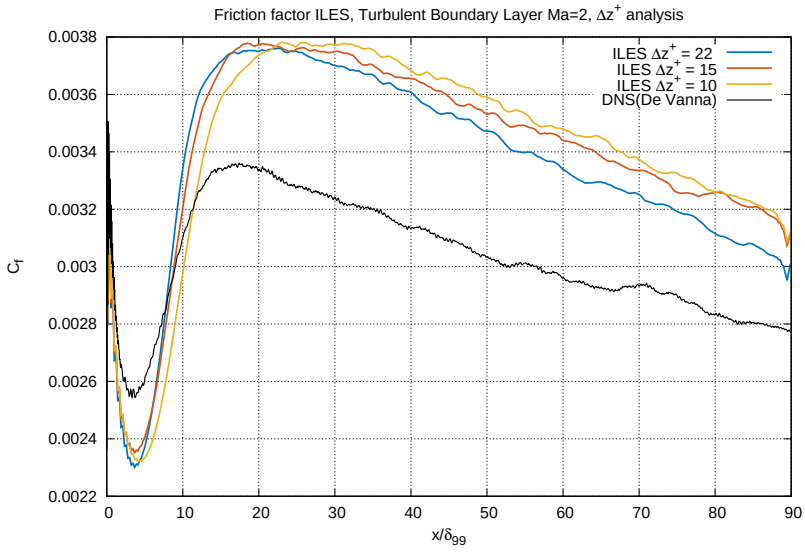

Figure 8.18: Friction factor with different grid resolutions along z

Figure (8.17) and figure (8.18) show that, with reference to the Δx^+ analyses (figures (8.11) and (8.12)), the increasing of the grid resolution along the z-axis determines a reduction of accuracy in the estimate of both friction factor and Re_τ.
This may be due to an excessive difference between the values of Δx^+ and Δz^+ used in these simulations.

8.2 Wall Modelled Boundary Layer Analyses

8.2.1 Comparison of results about analyses of the grid resolution along the y-axis

In the next figures, profiles of non-dimensional streamwise mean velocity and Reynolds stress along the wall-normal direction are summarised, for the analyses of grid resolution along the wall-normal direction.
For each resolution case, graphics of stations related to $Re_\tau = 200, 252$ are proposed, and both AWS and DWS results are compared to DNS data.

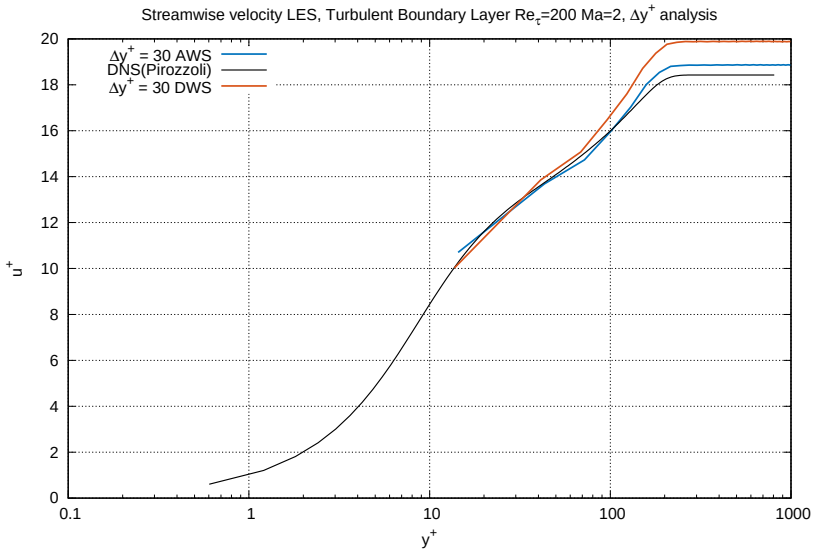

Figure 8.19: Comparison of mean velocity profiles of aws and dws models with $\Delta y^+ = 30$ related to Re_τ = 200

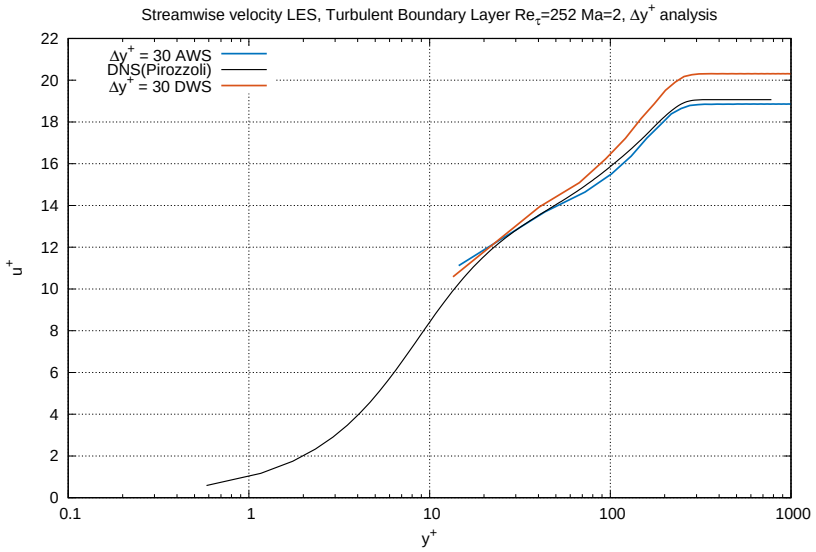

Figure 8.20: Comparison of mean velocity profiles of aws and dws models with $\Delta y^+ = 30$ related to Re_τ = 252

Mean streamwise velocity profiles related to $\Delta y^+ = 30$ of figures 8.19 and 8.20 show that the two models lead to data that are consistent with DNS results.
The DWS model tends to overestimate the velocity in the outer layer, especially for $Re_\tau = 200$, while the AWS model seems to be more accurate.
A possible reason could be the choice of taking the second LES-grid node from the wall to get the input data for the DWS wall-model, instead of the third one as it's implemented for the AWS model. Hence, this may lead to greater errors (see section 6.1).

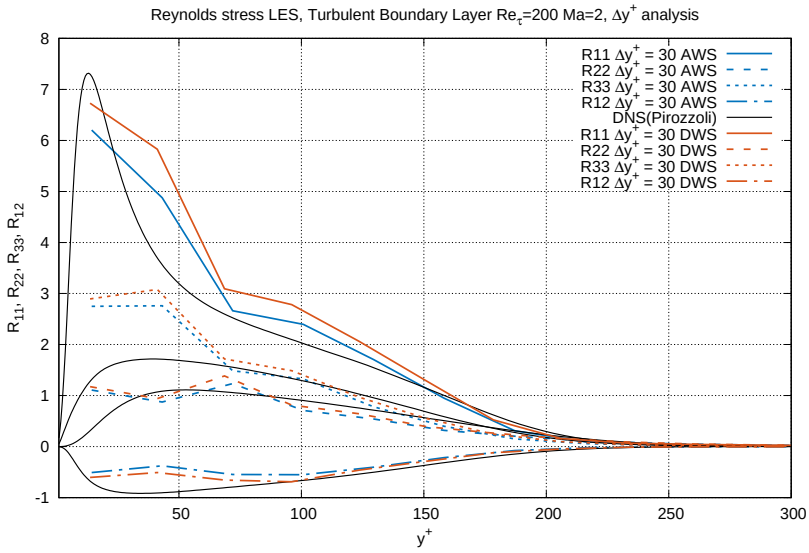

Figure 8.21: Comparison of Reynolds stress profiles of AWS and DWS models with $\Delta y^+ = 30$ related to Re_τ = 200

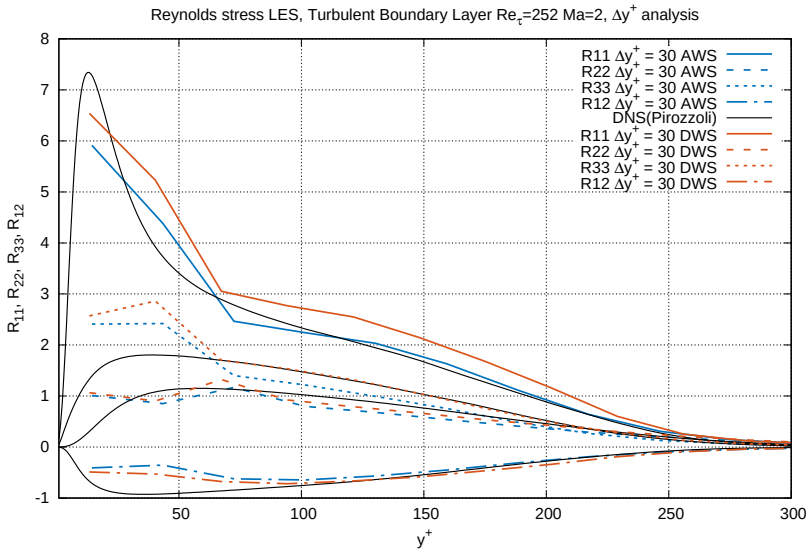

Figure 8.22: Comparison of Reynolds stress profiles of AWS and DWS models with $\Delta y^+ = 30$ related to Re_τ = 252

Figures 8.21 and 8.22 display a very decent trend of Reynolds stress into the outer layer for both the models.
In particular, $< v'^2 >, < w'^2 >$ and $< u'v' >$ components are almost coincident with DNS data for

both the models, while the $< u'^2 >$ is a bit overestimated by the DWS model.
It's worth noting that results related to $Re_\tau = 252$ are much better than the others. This is due to the fact that the $Re_\tau = 200$ value is associated to a coordinate very close to the inflow condition: so, this may distort the respective data.
Let us consider a notice on the trend into the inner layer.
Here the Reynolds stress profiles are not consistent with DNS data, because the wall-resolution is really far from what is needed to solve the dynamics in such region.
Therefore, trends can't be similar into this layer.
The goal of the wall model is thus to 'adjust' the shear stress and thermal flow boundary conditions, in order to get the correct dynamics over the modelled layer.
The next figures are related to the case with $\Delta y^+ = 20$.

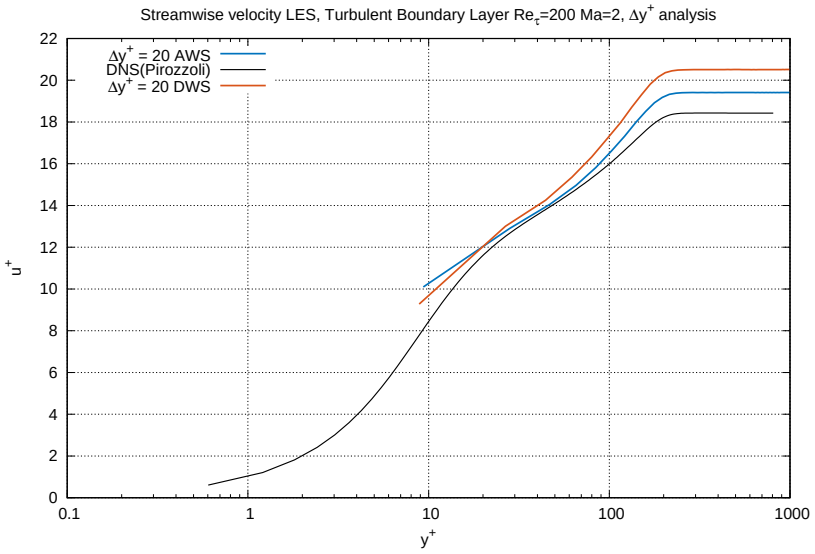

Figure 8.23: Comparison of mean velocity profiles of AWS and DWS models with $\Delta y^+ = 20$ related to Re_τ = 200

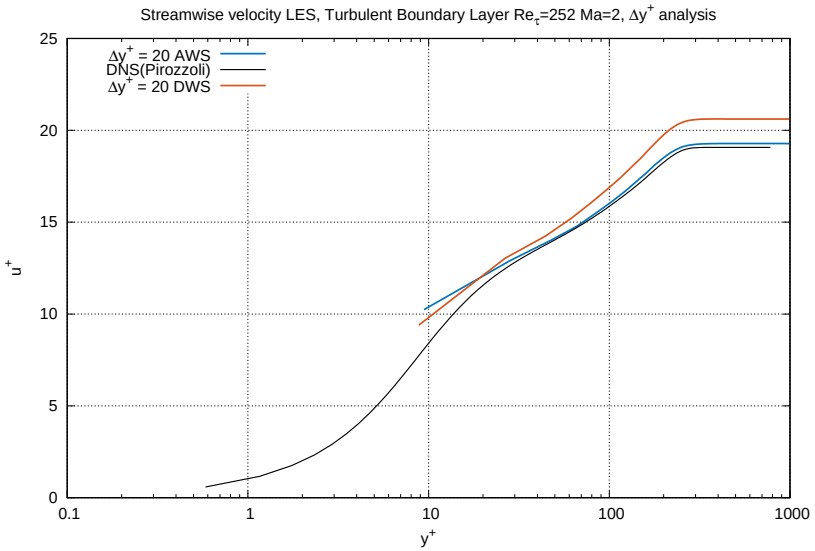

Figure 8.24: Comparison of mean velocity profiles of AWS and DWS models with $\Delta y^+ = 20$ related to Re_τ = 252

Figures 8.23 and 8.24 show that by increasing the resolution along the wall-normal direction improves the accuracy of results.
So, both the models are working properly.
As in the previous case, the profiles appear overestimated by the DWS model.

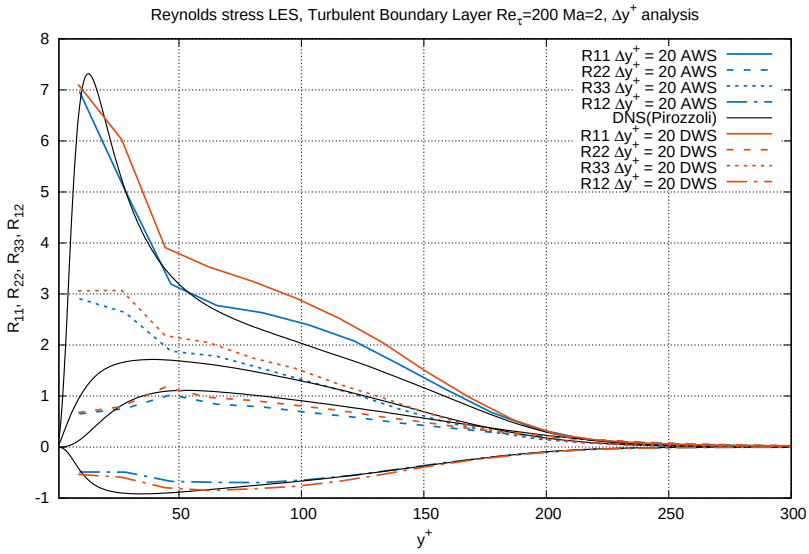

Figure 8.25: Comparison of Reynolds stress profiles of AWS and DWS models with $\Delta y^+ = 20$ related to Re_τ = 200

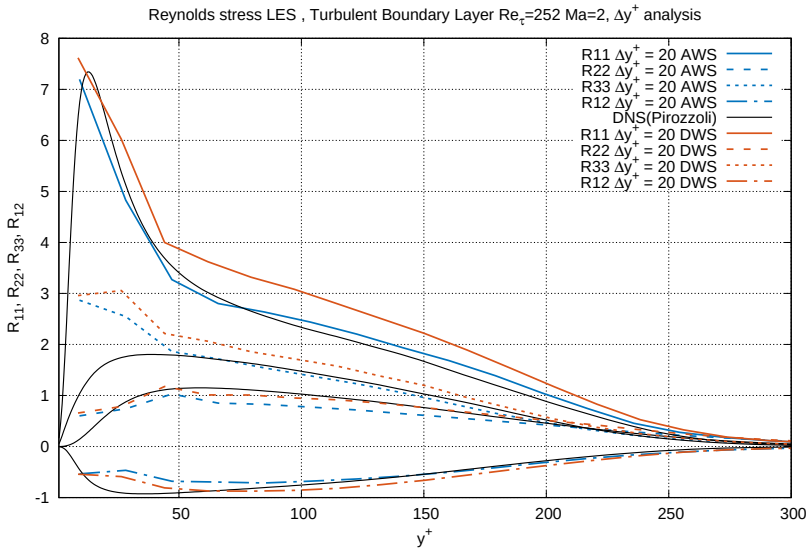

Figure 8.26: Comparison of Reynolds stress profiles of AWS and DWS models with $\Delta y^+ = 20$ related to Re_τ = 252

Figures 8.25 and 8.26 confirm what was said previously.
In particular, in this case results are really close to the correct ones, especially with the AWS model (see figure 8.26).

Next figures are related to the case of $\Delta y^+ = 40$.

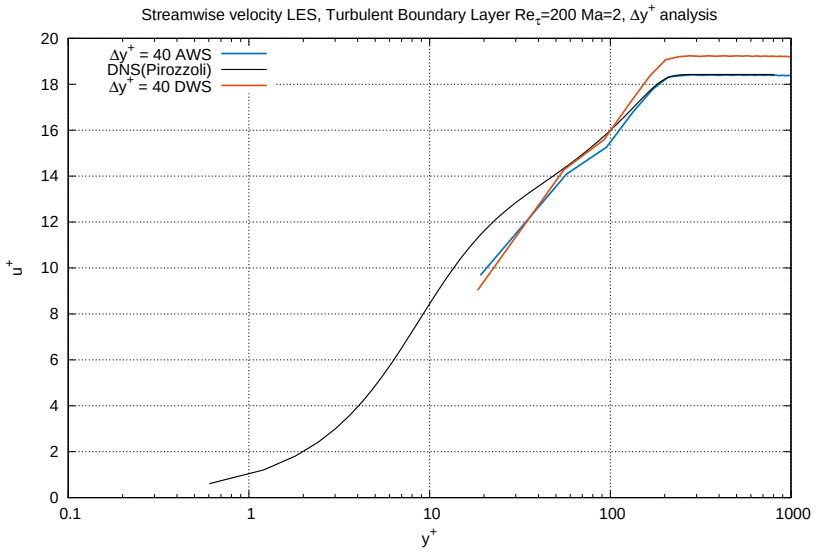

Figure 8.27: Comparison of mean velocity profiles of AWS and DWS models with $\Delta y^+ = 40$ related to Re_τ = 200

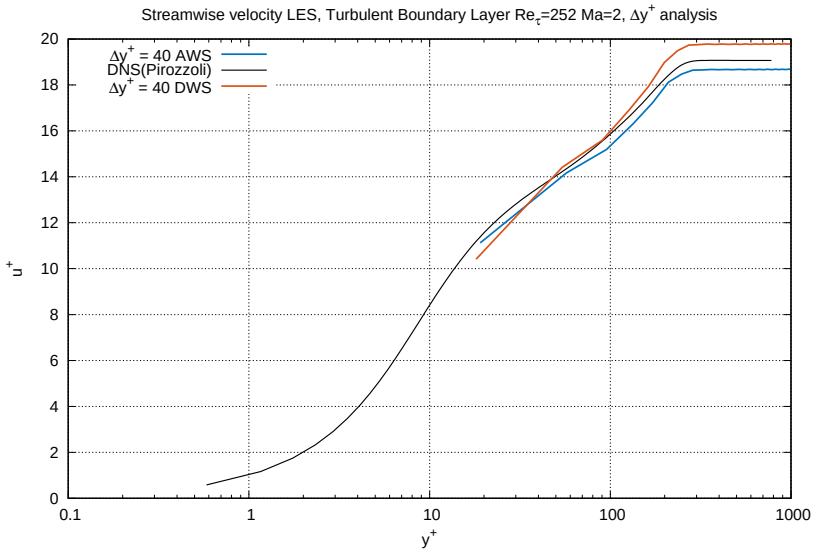

Figure 8.28: Comparison of mean velocity profiles of AWS and DWS models with $\Delta y^+ = 40$ related to Re_τ = 252

Figures 8.27 and 8.28 display that the mean velocity profiles remain coherent with DNS data also with a lower grid resolution.

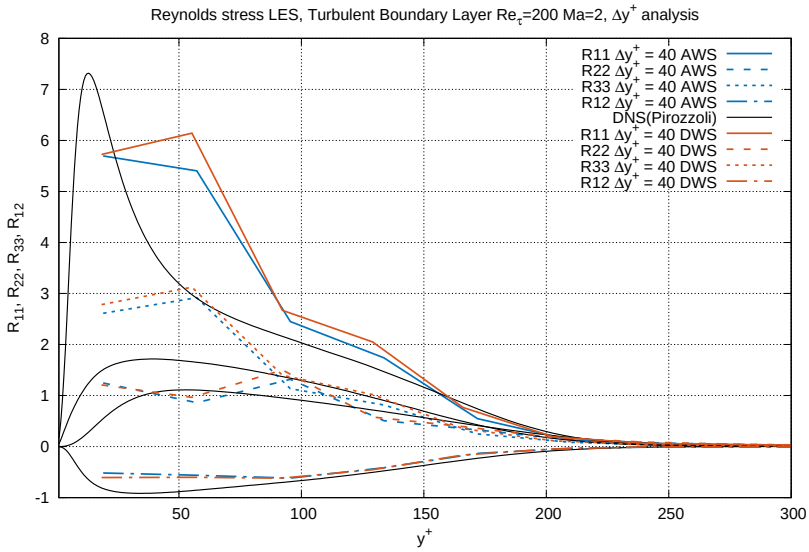

Figure 8.29: Comparison of Reynolds stress profiles of AWS and DWS models with $\Delta y^+ = 40$ related to Re_τ = 200

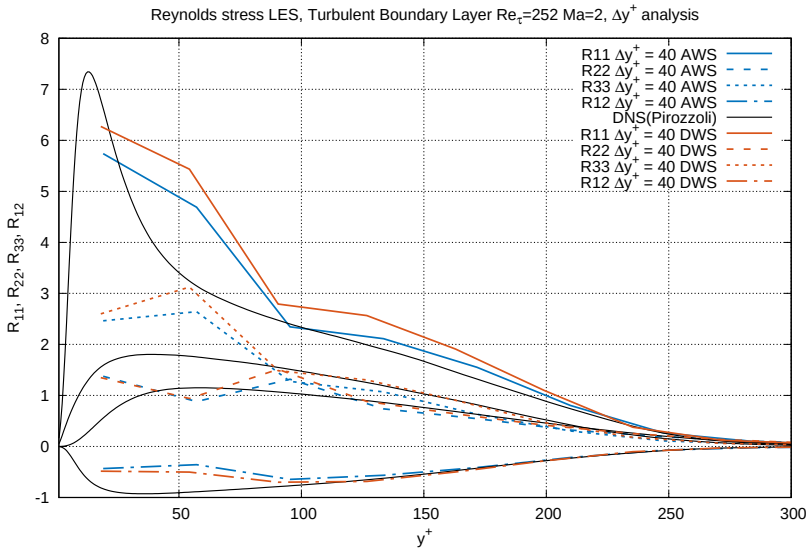

Figure 8.30: Comparison of Reynolds stress profiles of AWS and DWS models with $\Delta y^+ = 40$ related to Re_τ = 252

Graphics with Reynolds stress in figures 8.29 and 8.30 are of course less accurate than the previous ones.
In particular, it is underlined what has been said for low accuracy in the inner layer.
Results show trends that are very different compared to DNS ones for $y^+ < 100$, but almost coincident in the outer layer.

Chapter 9

Data fields

9.1 3D vorticity field

In this chapter several figures are proposed to show in detail the flow analysed in this work.
Figure (9.1) highlights the eddies and the turbulence of the boundary layer in the three-dimensional space.

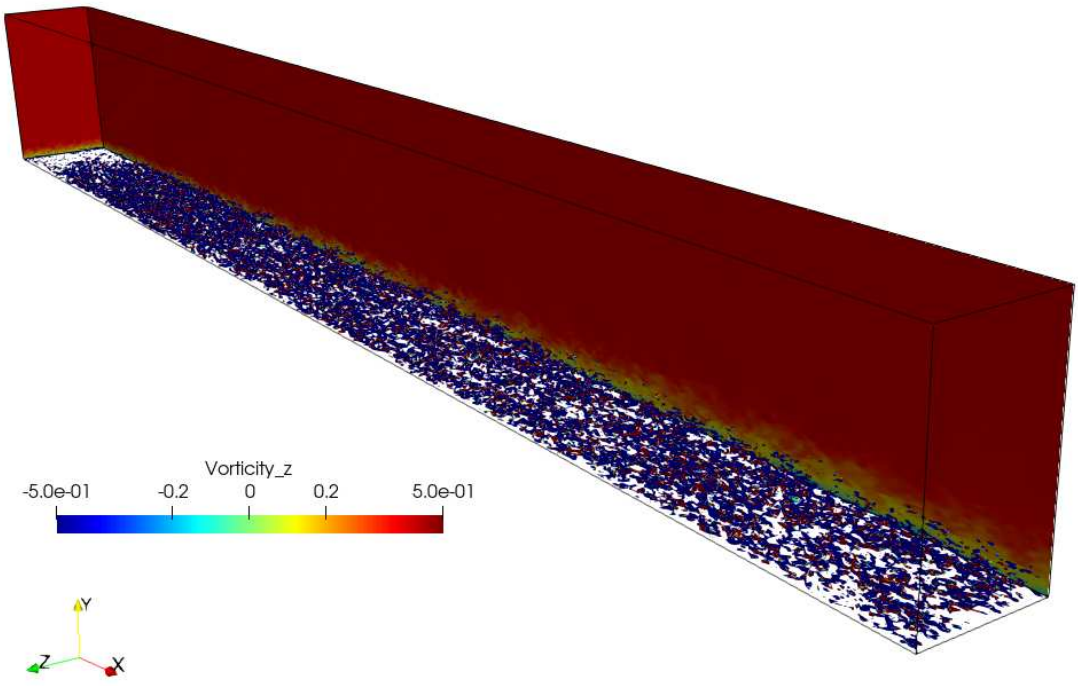

Figure 9.1: Visualisation of the simulation of the boundary layer at Re_τ=180.
Here the Q-criterion shows the 0.7 iso-contours of the second invariant of the velocity-gradient.
The colour map refers to the non-dimensional z-vorticity component.

9.2 2D velocity fields

The following figures display some slices of the velocity field.
In particular, fields of both WRLES and WMLES simulations are compared.

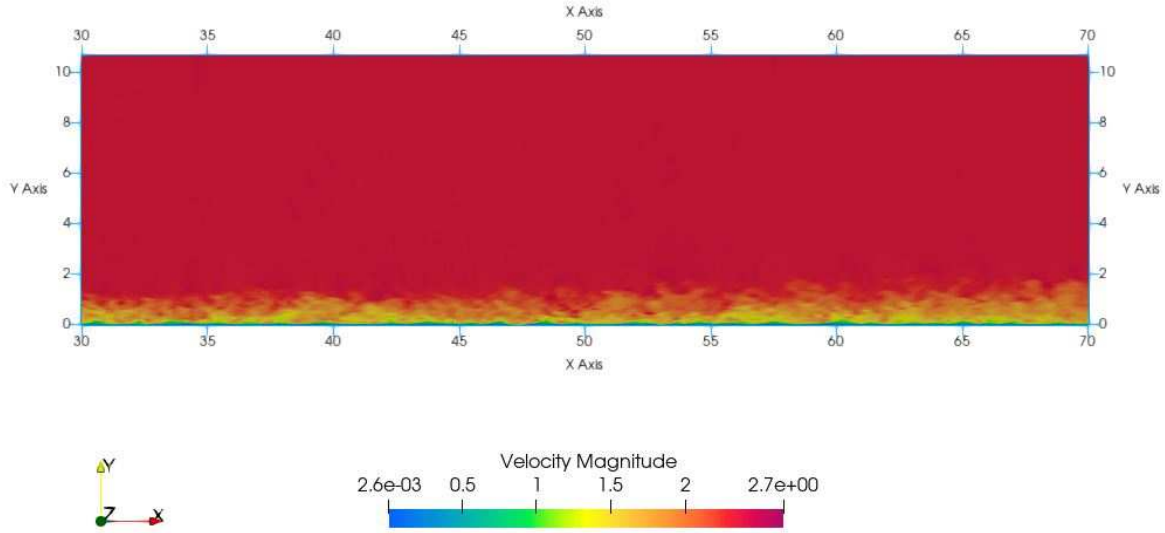

Figure 9.2: Visualisation of the velocity contour of the boundary layer at Re_τ=180 solved with WRLES approach.
The colour map refers to the non-dimensional velocity magnitude.
Data are considered far from the inflow and the outflow, within the range $x^+ = 30 \div 70$

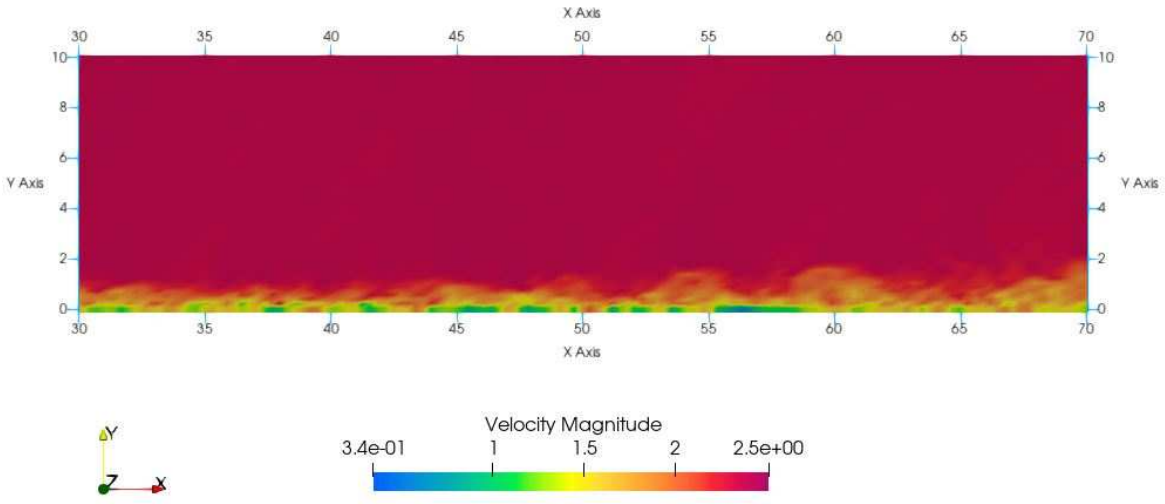

Figure 9.3: Visualisation of the velocity contour of the boundary layer at Re_τ=180 solved with WMLES approach.
The colour map refers to the non-dimensional velocity magnitude.
Data are considered far from the inflow and the outflow, within the range $x^+ = 30 \div 70$

9.3 2D temperature fields

The following figures display some slices of temperature fields.
As in the previous case, the comparison between WRLES and WMLES is proposed.

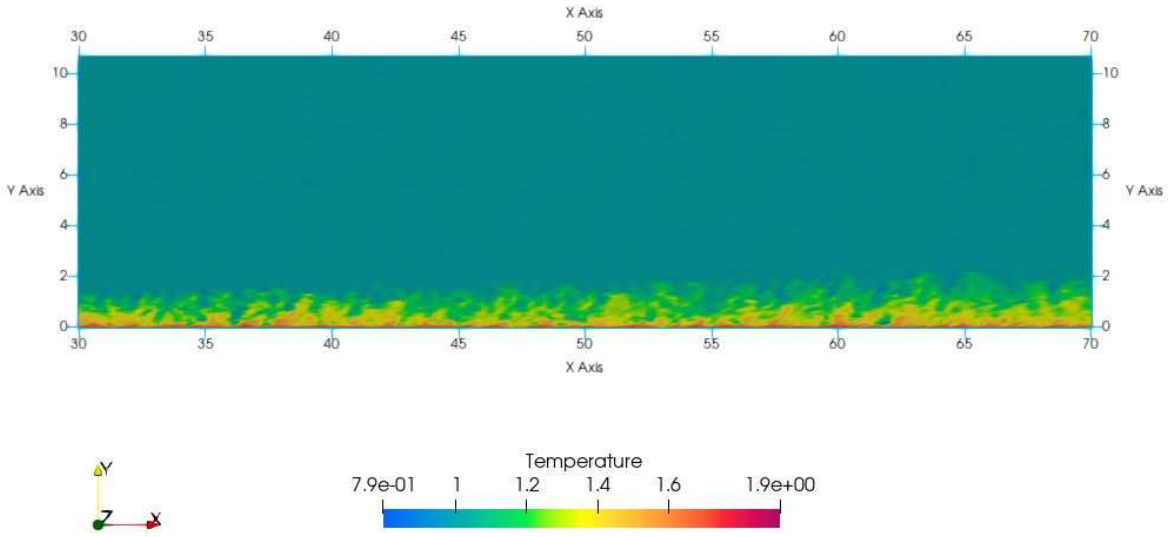

Figure 9.4: Visualisation of the static temperature of the boundary layer at Re_τ=180 solved with WRLES approach.
The colour map refers to the non-dimensional static temperature.
Data are considered far from the inflow and the outflow, within the range $x^+ = 30 \div 70$

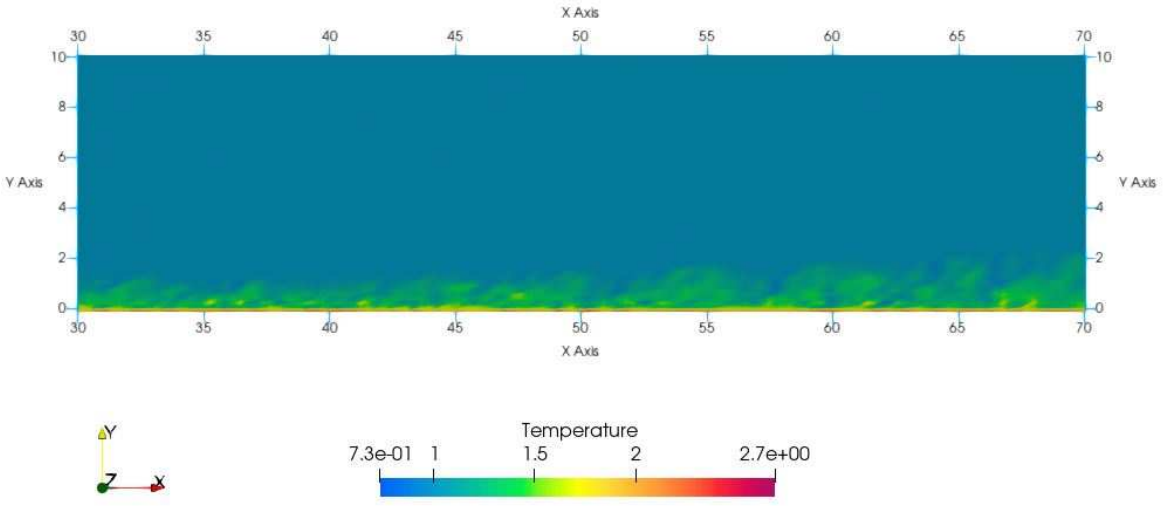

Figure 9.5: Visualisation of the static temperature contour of the boundary layer at Re_τ=180 solved with WMLES approach.
The colour map refers to the non-dimensional static temperature magnitude.
Data are considered far from the inflow and the outflow, within the range $x^+ = 30 \div 70$

9.4 2D vorticity fields

The following figures display some slices of the z-component of vorticity field.
Even in this case, data of WRLES and WMLES are proposed.

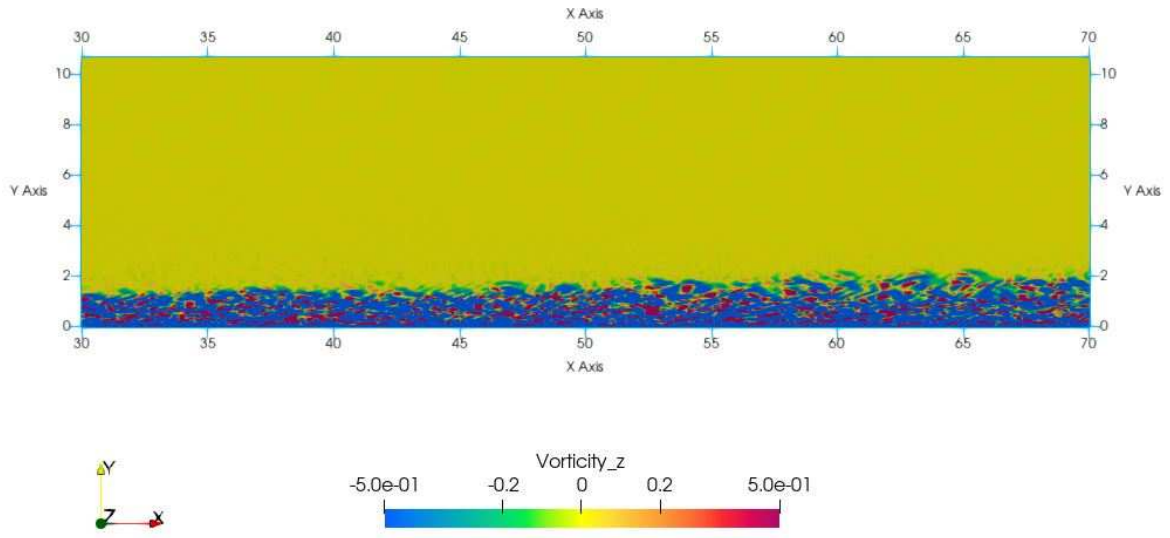

Figure 9.6: Visualisation of the vorticity contour of the boundary layer at Re_τ=180 solved with WRLES approach.
The colour map refers to the non-dimensional z-vorticity component.
Data are considered far from the inflow and the outflow, within the range $x^+ = 30 \div 70$

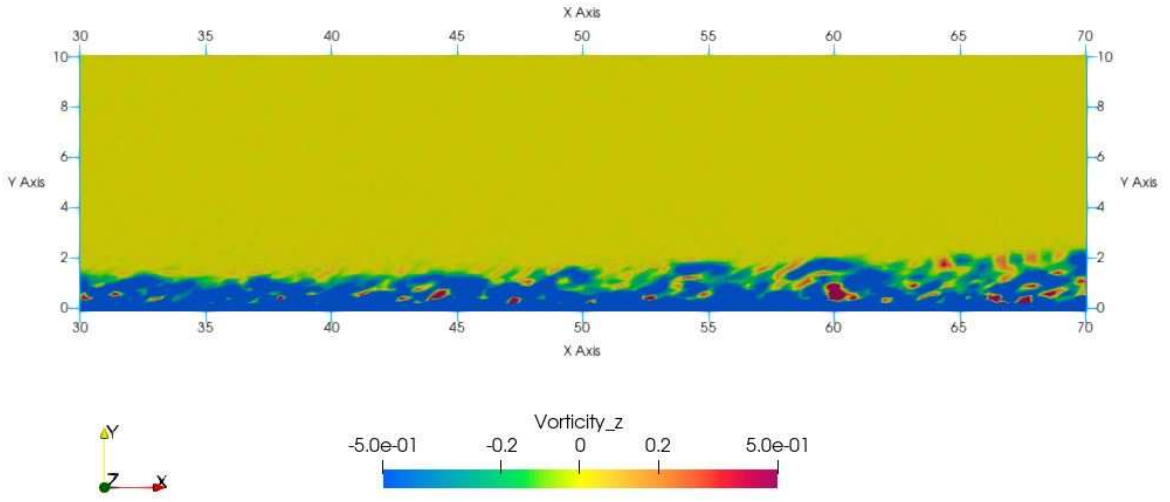

Figure 9.7: Visualisation of the vorticity contour of the boundary layer at Re_τ=180 solved with WMLES approach.
The colour map refers to the non-dimensional z-vorticity component.
Data are considered far from the inflow and the outflow, within the range $x^+ = 30 \div 70$

Chapter 10

Summary and conclusions

This thesis aims to study the wall turbulence by analysing the simplest wall flow in this framework, that is, the boundary layer on a flat plate.
So, several LES simulations have been performed considering supersonic and turbulent conditions, varying the grid and domain features and trying to point out the vortical structures near the wall.
In particular, with a wall-resolved approach the influnece of the grid resolution along streamwise and spanwise directions and the spanwise size of the domain has been tested.
Results have been compared to those related to DNS, found by Pirozzoli.
What can be seen from the study is the strong sensitivity of the solution accuracy as the resolution grid varies along streamwise and spanwise directions, converging towards correct data as the resolution increases.
Such influence is obviously related to the correct simulation of streaks, that govern the dynamics next to the wall.
From the streamwise resolution analyses we can observe a sensible variation that involves both the mean velocity profile and the Reynolds stress trends, especially for the $< u'^2 >$ component.
Concerning the spanwise resolution analysis, the increment of resolution influences significantly the Reynolds stress, but it seems not to affect the mean velocity profile.
On the other hand, we emphasise the almost independence of the solution as the domain size increases along the spanwise direction.
Hence, the eddies dynamics description next to the wall is already accurate with reasonably small spanwise size.
Regarding the WMLES analyses, results obtained with the algebraic wall-stress model are consistent with the DNS ones.
In particular, very accurate data have been observed for Reynolds stress in the outer layer for all the resolutions tested, and the mean velocity profiles are near the correct trend given by DNS.
Moreover, results tend to converge to DNS ones as the resolution increases. So, this validates the proposed model itself.
It's worth noting that data obtained with the algebraic wall-stress model appear more accurate than those ones related to DWS, both for the mean velocity profiles and Reynolds stress.
This could be due to the choice of getting the input data for the wall model from the third LES node instead of from the second one. So, it may minimise the respective errors.
It's important to notice that the solution times required for wall-modelled simulations are really shorter compared to the wall-resolved ones.
In particular, we have a reduction of about 70 %.
Hence, this work appears really interesting, with particular reference to the WMLES results.
Such technique is confirmed as really promising in the wall turbulence field, thanks to significant results related to a decent ratio between results quality and simulation time.
It can be considered as the unique approach that could be applicable in an industrial context in the near future, together with the RANS one, which is already being used.

Indeed, by means of the today's available computing powers, simulation times related to DNS and traditional LES approaches are still too high compared to the demands of a company business, which instead could be satisfied by means of a WMLES technique.

Appendix A

Incompressible boundary layer equations

Let's consider a stationary bi-dimensional incompressible flow with free-stream velocity U_∞ along the x direction that interacts with a body of characteristic size L.
We suppose that the Reynolds number $Re = \frac{U_\infty L}{\nu} \gg 1$.
We assume a body surface with a curvature small enough to be considered approximately parallel to the x direction, with y direction tat is normal to the surface itself. So, the velocity field **U** consists of two components, u(x,y) and v(x,y), aligned with x and y, respectively.
Such system can be described by the following Navier-Stokes equations [37]:

$$\frac{\partial u}{\partial x} + \frac{\partial v}{\partial y} = 0 \tag{A.0.1}$$

$$u\frac{\partial u}{\partial x} + v\frac{\partial u}{\partial y} = -\frac{1}{\rho}\frac{\partial p}{\partial x} + \nu\Big(\frac{\partial^2 u}{\partial x^2} + \frac{\partial^2 u}{\partial y^2}\Big) \tag{A.0.2}$$

$$u\frac{\partial v}{\partial x} + v\frac{\partial v}{\partial y} = -\frac{1}{\rho}\frac{\partial p}{\partial y} + \nu\Big(\frac{\partial^2 v}{\partial x^2} + \frac{\partial^2 v}{\partial y^2}\Big) \tag{A.0.3}$$

$$\rho u\frac{\partial h}{\partial x} + \rho v\frac{\partial h}{\partial y} = u\frac{\partial p}{\partial x} + v\frac{\partial p}{\partial y} + \frac{\mu}{Pr}\Big(\frac{\partial^2 h}{\partial x^2} + \frac{\partial^2 h}{\partial y^2}\Big) + 2\mu\Big[\Big(\frac{\partial u}{\partial x}\Big)^2 + \Big(\frac{\partial v}{\partial y}\Big)^2 + \Big(\frac{\partial u}{\partial y} + \frac{\partial v}{\partial x}\Big)^2\Big] \tag{A.0.4}$$

where the last one is the energy equation in terms of static enthalpy.

We want to find the inner solution (that is, the boundary layer solution) which connects the external solution with the adherence condition at the wall.
Hence, it's convenient to zoom in the region next to the body, where the viscous effects are significant. Defining with δ its thickness, we need to estimate how large is δ compared to L as a function of the Reynolds number, Re, in order to impose the appropriate change of variables.
By means of a dimensional analysis [25], we can assume that:

$$u\frac{\partial u}{\partial x} \sim \frac{U_\infty^2}{L} \tag{A.0.5}$$

$$\nu\frac{\partial^2 u}{\partial x^2} \sim \nu\frac{U_\infty}{L^2} \tag{A.0.6}$$

$$\nu\frac{\partial^2 u}{\partial y^2} \sim \nu\frac{U_\infty}{\delta^2} \tag{A.0.7}$$

where (A.0.5) denotes the dominant convective flux term, (A.0.6) and (A.0.7) indicate the diffusive terms, that must balance the momentum [1] introduced by (A.0.5).
It follows that:

[1] by slowing down the flow until the adherence condition is respected

$$\nu\frac{\partial^2 u}{\partial x^2}/u\frac{\partial u}{\partial x} \sim \frac{\nu}{U_\infty L} = \frac{1}{Re} \tag{A.0.8}$$

$$\nu\frac{\partial^2 u}{\partial y^2}/u\frac{\partial u}{\partial x} \sim \frac{\nu}{U_\infty L}\Big(\frac{L}{\delta}\Big)^2 = \frac{1}{Re}\Big(\frac{L}{\delta}\Big)^2 \tag{A.0.9}$$

If $Re \to \infty$, the ratio (A.0.8) is null. Thus, the term $\nu\partial^2 u/\partial x^2$ is negligible compared to $u\partial u/\partial x$ into the boundary layer.
The ratio (A.0.9) can be finite if $Re \to \infty$ only if $\delta/L \propto Re^{\frac{1}{2}}$. So, we can assume:

$$\frac{\delta}{L} = \frac{1}{\sqrt{Re}} \tag{A.0.10}$$

From the dimensional analysis of the terms of the continuity condition, we have:

$$\frac{\partial u}{\partial x} \sim \frac{U_\infty}{L} \tag{A.0.11}$$

$$\frac{\partial v}{\partial y} \sim \frac{V_\infty}{\delta} \tag{A.0.12}$$

These two terms are comparable only if:

$$\frac{V_\infty}{\delta}/\frac{U_\infty}{L} \sim 1 \tag{A.0.13}$$

It follows that:

$$V_\infty = \frac{U_\infty}{\sqrt{Re}} \tag{A.0.14}$$

Therefore, equations (A.0.10) and (A.0.14) are the relations that we want to test to obtain the boundary layer equations.
Let's consider the incompressible 2D Navier-Stokes equations:

$$\frac{\partial u^*}{\partial x^*} + \frac{\partial v^*}{\partial y^*} = 0 \tag{A.0.15}$$

$$u^*\frac{\partial u^*}{\partial x^*} + v^*\frac{\partial u^*}{\partial y^*} = -\frac{\partial p^*}{\partial x^*} + \frac{1}{Re}\Big(\frac{\partial^2 u^*}{\partial x^{*2}} + \frac{\partial^2 u^*}{\partial y^{*2}}\Big) \tag{A.0.16}$$

$$u^*\frac{\partial v^*}{\partial x^*} + v^*\frac{\partial v^*}{\partial y^*} = -\frac{\partial p^*}{\partial y^*} + \frac{1}{Re}\Big(\frac{\partial^2 v^*}{\partial x^{*2}} + \frac{\partial^2 v^*}{\partial y^{*2}}\Big) \tag{A.0.17}$$

$$u^*\frac{\partial h^*}{\partial x^*} + v^*\frac{\partial h^*}{\partial y^*} = u^*\frac{\partial p^*}{\partial x^*} + v^*\frac{\partial p^*}{\partial y^*} + \frac{1}{RePr}\Big(\frac{\partial^2 h^*}{\partial x*^2} + \frac{\partial^2 h^*}{\partial y*^2}\Big) + \frac{2}{Re}\Big[\Big(\frac{\partial u^*}{\partial x^*}\Big)^2 + \Big(\frac{\partial v^*}{\partial y^*}\Big)^2 + \Big(\frac{\partial u^*}{\partial y^*} + \frac{\partial v^*}{\partial x^*}\Big)^2\Big] \tag{A.0.18}$$

where $x^* = x/L$, $y^* = y/L$, $u^* = u/U_\infty$, $v^* = v/U_\infty$, $p^* = p/(\rho U_\infty)^2$, $h^* = h/U_\infty^2$. It's convenient to apply the change of variables, in order to zoom in what happens along only the y direction.
In particular:

$$y' = \frac{y}{\delta} = \frac{y}{L}\frac{L}{\delta} = y^*\sqrt{Re} \tag{A.0.19}$$

$$x' = \frac{x}{L} = x^* \tag{A.0.20}$$

$$u' = u^* = \frac{u}{U_\infty} \tag{A.0.21}$$

$$v' = v^*\sqrt{Re} = \frac{v}{U_\infty}\frac{U_\infty}{V_\infty} \tag{A.0.22}$$

$$p' = p^* \tag{A.0.23}$$

$$h' = h^* \tag{A.0.24}$$

Consequently, non-dimensional equations of continuity and y-momentum become:

$$\frac{\partial u'}{\partial x'} + \frac{\partial v'}{\partial y'} = 0 \tag{A.0.25}$$

$$\frac{1}{Re}\Big(u'\frac{\partial v'}{\partial x'} + v'\frac{\partial v'}{\partial y'}\Big) = -\frac{\partial p'}{\partial y'} + \frac{1}{Re^2}\frac{\partial^2 v'}{\partial x'^2} + \frac{1}{Re}\frac{\partial^2 v'}{\partial y'^2} \tag{A.0.26}$$

If $Re \to \infty$, the y-momentum equation is reduced to $\frac{\partial p'}{\partial y'} = 0$, that is, $p' = p'(x')$.
This means that the pressure into the boundary layer does not depend on the y coordinate for large Re number.
The junction condition for pressure is:

$$\lim_{y'\to\infty} p'(x') = \lim_{y^*\to 0} p_e^*(x^*, y^*) = p_{e,0}^*(x^*) = p'_{e,0}(x') \tag{A.0.27}$$

By introducing such information into the non-dimensional x-momentum equation, we have:

$$u'\frac{\partial u'}{\partial x'} + v'\frac{\partial u'}{\partial y'} = -\frac{\partial p'}{\partial x'} + \frac{1}{Re}\frac{\partial^2 u'}{\partial x'^2} + \frac{\partial^2 u'}{\partial y'^2} \tag{A.0.28}$$

If $Re \to \infty$, it becomes:

$$u'\frac{\partial u'}{\partial x'} + v'\frac{\partial u'}{\partial y'} = -\frac{dp'_{e,0}}{dx'} + \frac{\partial^2 u'}{\partial y'^2} \tag{A.0.29}$$

For the energy equation we have:

$$u'\frac{\partial h'}{\partial x'} + v'\frac{\partial h'}{\partial y'} = u'\frac{dp'_{e,0}}{dx'} + \frac{1}{Pr}\frac{\partial^2 h'}{\partial y'} + \Big(\frac{\partial u'}{\partial y'}\Big)^2 \tag{A.0.30}$$

In conclusion, the governing equations for incompressible boundary layer are:

$$\frac{\partial u'}{\partial x'} + \frac{\partial v'}{\partial y'} = 0 \tag{A.0.31}$$

$$\frac{\partial p'}{\partial y'} = 0 \tag{A.0.32}$$

$$u'\frac{\partial u'}{\partial x'} + v'\frac{\partial u'}{\partial y'} = -\frac{dp'_{e,0}}{dx'} + \frac{\partial^2 u'}{\partial y'^2} \tag{A.0.33}$$

$$u'\frac{\partial h'}{\partial x'} + v'\frac{\partial h'}{\partial y'} = u'\frac{dp'_{e,0}}{dx'} + \frac{1}{Pr}\frac{\partial^2 h'}{\partial y'} + \Big(\frac{\partial u'}{\partial y'}\Big)^2 \tag{A.0.34}$$

These equations lend two boundary conditions for the u' component of the flow:

$$u'(x', y' = 0) = 0 \qquad \text{adherence condition} \tag{A.0.35}$$

$$\lim_{y'\to\infty} = U_{e,0}^*(x) \qquad \text{junction condition} \tag{A.0.36}$$

and one boundary condition for the v' component:

$$v'(x', y' \to 0) = 0 \qquad \text{impermeability condition} \qquad \text{(A.0.37)}$$

Appendix B

Mechanical and thermal energy equations

From the momentum conservation equation associated to a generic flow it's possible to obtain a scalar equation usually called *mechanical energy equation*.
By doing the scalar product between the momentum conservation equation and the velocity **v**, you have [36]:

$$\rho \mathbf{v} \frac{D\mathbf{v}}{Dt} = -\mathbf{v} \cdot \nabla p + \mathbf{v} \cdot (\nabla \cdot \tau) + \rho \mathbf{v} \cdot \mathbf{g} \tag{B.0.1}$$

It's possible to prove that the first term of equation (B.0.1) is:

$$\rho \mathbf{v} \frac{D\mathbf{v}}{Dt} = \rho \frac{D}{Dt}\Big(\frac{1}{2} v^2\Big) \tag{B.0.2}$$

that is, the total derivative of the kinetic energy of the unit volume.
Since

$$-\rho \mathbf{v} \cdot \mathbf{g} = \rho \frac{D}{Dt}(gh) \tag{B.0.3}$$

equation (B.0.1) can be written as:

$$\rho \frac{D}{Dt}\Big(\frac{1}{2} v^2 + gh\Big) = -\mathbf{v} \cdot \nabla p + \mathbf{v} \cdot (\nabla \cdot \tau) \tag{B.0.4}$$

This last equation shows the relation between the mechanical energy variations (kinetic and gravitational ones) and the forces that act on the control volume surface.
The total energy conservation equation is:

$$\rho \frac{D}{Dt}\Big(e + \frac{1}{2} v^2 + gh\Big) = -\nabla \cdot \mathbf{q} - \nabla \cdot (p\mathbf{v}) + \nabla(\tau \mathbf{v}) \tag{B.0.5}$$

and can be expressed by expanding $\nabla \cdot (p\mathbf{v}) + \nabla(\tau\mathbf{v})$ as:

$$\rho \frac{D}{Dt}\Big(e + \frac{1}{2} v^2 + gh\Big) = -\nabla \cdot \mathbf{q} - p\nabla \cdot \mathbf{v} - \mathbf{v} \cdot \nabla p + \mathbf{v} \cdot (\nabla \cdot \tau) + \tau : \nabla \mathbf{v} \tag{B.0.6}$$

By subtracting equation (B.0.4) from (B.0.6) we have:

$$\rho \frac{De}{Dt} = -\nabla \cdot \mathbf{q} - p\nabla \cdot \mathbf{v} + \tau : \nabla \mathbf{v} \tag{B.0.7}$$

This equation can be called *thermal energy equation*, since it permits to evaluate the temperature variations due to heat flux for conduction ($\nabla \cdot \mathbf{q}$), reversible compression ($p\nabla \cdot \mathbf{v}$) and irreversible viscous dissipation ($\tau : \nabla \mathbf{v}$).

These last two terms represent the conversion from mechanical energy to thermal energy.
For a Newtonian fluid the viscous dissipation term $\tau : \nabla \mathbf{v}$ can be expressed as:

$$\tau : \nabla \mathbf{v} = \mu \Phi_v = 2\mu \Big\{ \Big(\frac{\partial u}{\partial x}\Big)^2 + \Big(\frac{\partial v}{\partial y}\Big)^2 + \Big(\frac{\partial w}{\partial z}\Big)^2 + \frac{1}{2}\Big[\Big(\frac{\partial v}{\partial x} + \frac{\partial u}{\partial y}\Big)^2 + \Big(\frac{\partial w}{\partial y} + \frac{\partial v}{\partial z}\Big)^2 + \Big(\frac{\partial u}{\partial z} + \frac{\partial w}{\partial x}\Big)^2 \Big] + \\ + \frac{1}{3}\Big(\frac{\partial u}{\partial x} + \frac{\partial v}{\partial y} + \frac{\partial w}{\partial z}\Big)^2 \Big\} \quad \text{(B.0.8)}$$

where Φ_v is the viscous dissipation function.

Viscous dissipation determines an increase of the fluid temperature that in practical applications is often negligible.

Appendix C

The turbulent Crocco-Busemann relation

We want to obtain an equation for the temperature profile into a bi-dimensional compressible turbulent boundary layer.
Under the Morkovin's hypothesis [1], the boundary layer equations [40] are:

$$\frac{\partial}{\partial x}(\bar{\rho}\bar{u}) + \frac{\partial}{\partial y}(\overline{\rho v}) = 0 \qquad \text{Continuity} \qquad \text{(C.0.1)}$$

$$\bar{\rho}\bar{u}\frac{\partial \bar{u}}{\partial x} + \overline{\rho v}\frac{\partial \bar{u}}{\partial y} = \rho_\infty U_\infty \frac{dU_\infty}{dx} + \frac{\partial \tau}{\partial y} \qquad \text{x momentum} \qquad \text{(C.0.2)}$$

$$\frac{\partial \bar{p}}{\partial y} = -\frac{\partial}{\partial y}\overline{(\rho v' v')} \ll \left|\frac{\partial p}{\partial y}\right| \qquad \text{y momentum} \qquad \text{(C.0.3)}$$

$$\bar{\rho}\bar{u}\frac{\partial \bar{h}}{\partial x} + \overline{\rho v}\frac{\partial \bar{h}}{\partial y} = \bar{u}\frac{d\bar{p}}{dx} + \frac{\partial q}{\partial y} + \tau\frac{\partial \bar{u}}{\partial y} \qquad \text{Energy} \qquad \text{(C.0.4)}$$

$$\text{(C.0.5)}$$

where:

$$\tau = \bar{\mu}\frac{\partial \bar{u}}{\partial y} - \overline{\rho u' v'} \qquad \text{(C.0.6)}$$

$$q = \bar{\lambda}\frac{\partial \bar{T}}{\partial y} - \overline{\rho v' h'} \qquad \text{(C.0.7)}$$

As for incompressible flow, there is a slight pressure gradient in the y direction that can be ignored in the present context (hence, $\frac{\partial \bar{p}}{\partial x} \approx -\rho_\infty U_\infty \frac{dU_\infty}{dx}$).
Supposing the following definitions:

$$-\overline{\rho u' v'} = \mu_t \frac{\partial \bar{u}}{\partial y} \qquad \text{(C.0.8)}$$

$$-\overline{\rho v' h'} = \lambda_t \frac{\partial \bar{T}}{\partial y} \qquad \text{(C.0.9)}$$

where μ_t is the turbulent eddy viscosity and λ_t is the turbulent eddy conductivity, we can rewrite the momentum and the energy equations using the total enthalpy obtained with mean quantities $H = \bar{h} + \frac{\bar{u}^2}{2}$:

[1] which postulates that high-speed turbulence structure in zero pressure-gradient turbulent boundary layers remains largely the same as in incompressible counterpart [44]

$$\bar{\rho}\bar{u}\frac{\partial \bar{u}}{\partial x} + \overline{\rho v}\frac{\partial \bar{u}}{\partial y} = -\frac{d\bar{p}}{dx} + \frac{\partial}{\partial y}\Big[(\mu + \mu_t)\frac{\partial \bar{u}}{\partial y}\Big] \quad \text{x momentum} \tag{C.0.10}$$

$$\bar{\rho}\bar{u}\frac{\partial H}{\partial x} + \overline{\rho v}\frac{\partial H}{\partial y} = \frac{\partial}{\partial y}\Big[\Big(\frac{\mu}{\mathrm{Pr}} + \frac{\mu_t}{\mathrm{Pr}_t}\Big)\frac{\partial H}{\partial y}\Big] + \frac{\partial}{\partial y}\Big[\mu\Big(1 - \frac{1}{\mathrm{Pr}}\Big) + \mu_t\Big(1 - \frac{1}{\mathrm{Pr}_t}\Big)\Big]\frac{\partial}{\partial y}\Big(\frac{\bar{u}^2}{2}\Big) \quad \text{Energy} \tag{C.0.11}$$

where $Pr_t = \frac{\mu_t c_p}{\lambda_t}$ is the turbulent Prandtl number.

Under the reasonable assumption $Pr \approx Pr_t \approx 1$ (approximately true for air) and if the pressure gradient is negligible, the previous two equations are identical in mathematical form and a particular solution is

$$H = C_1 + C_2\bar{u} \tag{C.0.12}$$

or

$$H = C_1 + C_2\bar{u} - \frac{\bar{u}^2}{2} \tag{C.0.13}$$

When the boundary conditions T_w, U_∞ are introduced, we obtain

$$\bar{T} \approx T_w + (T_{aw} - T_w)\frac{\bar{u}}{U_\infty} - r\frac{\bar{u}^2}{2c_p} \tag{C.0.14}$$

Thus, the Crocco-Busemann relation between temperature and velocity is also valid with good accuracy for turbulent flows with a negligible pressure gradient.
It is also a good approximation with pressure gradients.
It's worth noting that we have assumed constant c_p (so that $\bar{h} \approx c_p\bar{T}$) and have slipped in the recovery factor, *r*, for greater accuracy.

Bibliography

[1] Strato limite compressibile. Lecture notes from a course of University of Rome 'La Sapienza'.

[2] L. Affonso. *Machinery Failure Analysis Handbook*. Gulf Publishing Company, 2007.

[3] H. Bai, Y. Zhou, W. Zhang, and R. Antonia. Streamwise vortices and velocity streaks in a locally drag-reduced turbulent boundary layer. *Flow Turbulence Combust*, pages 391–416, 2018.

[4] O. Ben-Nasr, A. Hadjadj, A. Chaudhuri, and M. Shadloo. Assessment of subgrid-scale modeling for large-eddy simulation of a spatially-evolving compressible turbulent boundary layer. *Computers and Fluids*, pages 144–158, 2017.

[5] M. Bull. Wall-pressure fluctuations beneath trbulent boundary layers: some reflections on forty years of research. *Journal of Sound and Vibration*, pages 299–315, 1996.

[6] F. De Vanna. A high resolution fully compressible navier-stokes solver for analysis of moving objects at high mach numbers, 2019.

[7] F. De Vanna. Appunti del corso di laboratorio di fluidodinamica computazionale. Notes from the CFD course in Università degli studi di Padova, 2020.

[8] F. De Vanna, F. Picano, and E. Benini. An immersed boundary method for moving objects in compressible flows. In *ERCOFTAC Workshop Direct and Large Eddy Simulation*, pages 291–296. Springer, 2019.

[9] F. De Vanna, F. Picano, and E. Benini. A sharp-interface immersed boundary method for moving objects in compressible viscous flows. *Computers & Fluids*, pages 104–415, 2020.

[10] E. Garnier, N. Adams, and P. Sagaut. *Large Eddy Simulation for Compressible Flows*. Springer, 2009.

[11] R. Guido. Blade profile loss model development for axial-flow fans and compressors performance prediction using through-flow simulations. Master's degree, Politecnico di Torino, 2018.

[12] S. Hojas and J. Jimenez. Reynolds number effects on the reynolds-stress budgets in turbulent channels. *Physics of Fluids*, 2008.

[13] J. Jimenez. Near-wall turbulence. *Physics of Fluids*, 2013.

[14] S. Kawai and J. Larsson. Wall-modeling in large eddy simulation: Legth scales, grid resolution, and accuracy. *Physics of Fluids*, 2012.

[15] Klein. A digital filter based generation of inflow data for spatially developing direct nmerical or largeeddy simulations. *Journal of Computational Physics*, 2003.

[16] S. Kline, W. Reynolds, F. Schraub, and P. Runstadler. The structure of turbulent boundary layers. *Journal of Fluid Mechanics*, pages 741–773, 1967.

[17] A. Laganelli, A. Martellucci, and L. Shaw. Wall pressure fluctuations in attached boundary-layer flow. *AIAA Journal*, pages 495–502, 1983.

[18] J. Larsson, S. Kawai, and I. Bermejo-Moreno. Large eddy simulation with modeled wall-stress: recent progress and future directions. *JSME*, 2016.

[19] L. Maxit and V. Denis. Prediction of flow induced sound and vibration of periodically stiffened plates. *Acoustical Society of America Journal*, 133:146, 2013.

[20] A. F. Molland, S. R. Turnock, and D. A. Hudson. *Ship resistance and propulsion*. Cambridge University Press, 2017.

[21] F. Nicoud and F. Ducros. Subgrid-scale stress modelling based on the square of the velocity gradient tensor. *flow turbulent combustion*, 1999.

[22] P. Orlandi and J. Jimenez. On the generation of turbulent wall friction. *Physics of Fluids*, pages 634–641, 1994.

[23] C. Ostoich, D. Bodony, and P. Geubelle. Interaction of a mach 2.25 turbulent boundary layer with a fluttering panel using direct numerical simulation. *Physics of Fluids*, 2013.

[24] F. Picano. In *LES*, 2020. Slides from Computational Fluid Dynamics Laboratory course of University of Padova.

[25] F. Picano. In *Strato limite 2*, 2020. Slides from Aerodynamic 2 course of University of Padova.

[26] F. Picano. Flussi ad alto numero di reynolds. Lecture notes from the Aerodynamics 2 course of University of Padova, 2020.

[27] U. Piomelli. Wall-layer models for large eddy simulations. *Prog. Aero. Sci.*, 44:437–446, 2008.

[28] U. Piomelli and E. Balaras. Wall-layer models for large eddy simulations. *Ann. Rev. Fluid. Mech.*, 34:349–374, 2002.

[29] S. Pirozzoli. 2017. http://reynolds.dma.uniroma1.it/dnsm2/stat.

[30] S. Pirozzoli and T. Colonius. Generalized characteristic relaxation boundary conditions for unsteady compressile flow simulations. *Journal of Computational Physics*, pages 109–126, 2013.

[31] K. Ritos, D. Drikakis, and I. Kokkinakis. Acoustic loading beneath hypersonic transitional and turbulent boundary layers. *Journal of Sound and Vibration*, pages 50–62.

[32] K. Ritos, I. Kokkinakis, D. Drikakis, and S. Spottswood. Implicit large eddy simulation of acoustic loading in supersonic turbulent boundary layers. *Physics of Fluids*, 2017.

[33] P. Sagaut. Large eddy simulation for incompressible flows. 2006.

[34] F. Schoppa, W.and Hussain. Coherent structure generation in near-wall turbulence. *Journal of Fluid Mechanics*, pages 57–108, 2002.

[35] S. M. Seyyedi, A. S. Dogonchi, M. Hashemi-Tilehnoee, and D. D. Ganji. Improved velocity and temperature profiles for integral solution in laminar boudary layer flow on a semi-infinite flat plate. 2018.

[36] A. Soldati. Corso di fuidodinamica e turbolenza. Raccolta di appunti delle lezioni del corso di fluidodinamica e turbolenza dell'università degli studi di Udine, 2008.

[37] L. Soldati. A numerical study on the shock wave boundary layer interaction. Master's degree, Università degli studi di Padova, 2020.

[38] P. Spalart. Detached-eddy simulation. *Ann. Rev. Fluid. Mech.*, 41:181–202, 2009.

[39] E. Van Driest. On turbulent flow near a wall. *Journal of Aero. Sci.*, pages 1007–1011, 1965.

[40] F. M. White. *Viscous Fluid Flow*. Mc Graw Hill Education, 2006.

[41] Xie. Efficient generation of inflow conditions for large eddy simulation of street-scale flows. *FT and C*, 2008.

[42] X. Xu. *Large eddy simulations of compressible turbulent pipe flow with heat transfer*. doctoral dissertation, 2003.

[43] X. I. A. Yang, J. Urzay, S. Bose, and P. Moin. Aerodynamic heating in wall-modeled large-eddy simulation of high-speed flows. *AIAA Journal*, 2018.

[44] C. Zhang. Direct numerical simulation of pressure fluctuations induced by supersonic turbulent boundary layers.

List of Figures

List of Tables